Interplay of stereo-electronic, vibronic and environmental effects in tuning the Chiroptical Properties of an Ir(III) Cyclometalated N-heterocyclic Carbene

Qin Yang, Marco Fusè, Julien Bloino, Vincenzo Barone*

Scuola Normale Superiore, Piazza dei Cavalieri 7, I-56126 Pisa, Italy

---

Abstract

Chiroptical spectra are among the most suitable techniques for investigating the ground and excited electronic states of chiral systems, but their interpretation is not straightforward and strongly benefits from quantum chemical simulations, provided that the employed computational model is sufficiently accurate and deals properly with stereo-electronic, vibrational averaging and environmental effects. Since the synergy among all these effects is only rarely accounted for, especially for large and flexible organometallic systems, the main aim of this contribution is to illustrate the latest developments of computational approaches rooted into the density functional theory for describing stereo-electronic effects and complemented by effective techniques to deal with vibrational modulation effects and solvatochromic shifts. In this connection, chiral iridium complexes offer an especially suitable case study in view of their bright phosphorescence, which is particularly significant for building effective light emitting diodes (OLEDs) and biomarkers and can be finely tuned by the nature of the metal ligands. In this connection, a recently synthesized family of cycloiridiated complexes, KC and KD, bearing a pentahelicenic N-heterocyclic carbene (KB), has shown an enhanced long-lasting, bright phosphorescence. Deeper insights

---

[☆] Fully documented templates are available in the elsarticle package on CTAN.

[*] Corresponding author

Email address: `vincenzo.barone@sns.it` (Vincenzo Barone)

into the still unclear nature and origin of the enhancement could be gained by the interpretation of the chiroptical spectra, which is quite challenging in view of the presence of two sources of chirality, the chiral center on Ir and the chiral axis related to the helicene ligand, in addition to the relativistic effects related to the presence of the Ir center. At the same time, the large dimensions of KC and KD hamper the use of the most sophisticated (but prohibitively expensive) computational models, so that more approximate approaches must be validated on a suitable model compound. To this end, after optimizing the computational scheme on a model system devoid of the helicene moiety (KA), we have performed a comprehensive investigation of the KC and KD spectra, whose interpretation is further aided by novel graphical tools. The discussion and analysis of the results will not be focused on the theoretical background, but, rather, on practical details (specific functional, basis set, vibronic model, solvent regime) with the aim of providing general guidelines for the use of last-generation computational spectroscopy tools also by non-specialists.

Keywords: Computational spectroscopy, Vibronic contributions,
Franck–Condon/Herzberg–Teller, N-heterocyclic carbene (NHC),
Ir-Complexes, Electronic circular dichroism, Circulary polarized luminescence,
Phosphorescence

---

1. Introduction

Computational spectroscopy has become a widespread tool for the interpretation of experimental results, and in some cases, also for their prediction, which becomes mandatory in a number of technological applications like fast screening procedures, or when experimental requirements are not practical or too expensive. Under some conditions, for instance when differentiating conformers or with highly sensitive techniques, it is mandatory to reach an unequivocal conclusion. The routine use of quantum chemical (QC) simulations beyond the community of theoretical chemists has been favored by the significant improvements reached over the recent years in terms of accuracy and efficiency, supported by more powerful and affordable hardware. However, the adoption rate of the more refined models is generally slow due to the delay of implementation of user-friendly interfaces in general-purpose programs, coupled to the difficulty of evaluating the applicability of different approaches to the cases of interest, and the perceived extra cost and complexity of the overall process with respect to the expected gain in accuracy.

Here, we will try to contribute to overcoming some of these difficulties in the specific case of electronic spectra in the UV-visible wavelength range. The seminal works of Franck[? ?] and Condon[? ?], completed by a series of derivations, notably by Sharp and Rosenstock[?] in the 1960's and later Doktorov[? ?] paved the way to general equations able to account in a cost-effective way for the vibrational modulation of UV-visible spectra.[? ? ? ? ? ?] During the last decade, several implementations of theoretical models to compute vibrationally-resolved electronic spectra, often shortened to vibronic spectra, have been reported, with different degrees of sophistication. [? ? ? ? ? ?] Yet, UV-visible spectra are still commonly simulated in terms of pure electronic transitions modulated by phenomenological line-shapes. Besides the obvious inability of reproducing spectra with visible vibronic structures,[? ? ?] such an approach can provide insufficient or misleading information for dipole-forbidden or weakly-allowed transitions, for instance when dealing with systems of high symmetry like porphyrins, or when tackling low-intensity,[?] resonance or non-linear spectroscopic techniques.[? ?]

In parallel to the improvement of theoretical models, a separate but complementary development activity has been devoted to the search for novel graphical representations, less focused on the final outcome, the spectra, and more on intermediate data and molecular physical-chemical properties.[? ? ? ? ? ?] When properly conceived and applied, such visual aids can greatly support the interpretation of band-shapes by providing some insight on the origin of the most significant features, as well as clues on possible structural improvements.[? ?]

The possibilities offered by these developments in terms of accuracy and insights are used here for the analysis of the chiroptical properties of an octahedral cyclometallated Iridium(III) complex bearing a N-heterocyclic carbene, which recently showed interesting phosphorescence property.[?]

Octahedral cyclometallated Ir(III) complexes have been extensively investigated in the last decades due their photophysical properties, that allow application in organic light-emitting devices (OLED), as well as in biological imaging.[? ? ? ?] Several enantiopure emitting cyclometallated Ir(III) complexes have been reported and chiroptically characterized.[? ? ? ? ?] In particular, the complexes investigated in Ref. [?] combine the iridium core with a NHC-based ligand achieving unusual light-green phosphorescence and circular polarization properties. The unprecedented features of the complexes have been attributed to the extensive π conjugation and to the interaction among the different moieties in the molecule. These characteristics combined with the vibrational structure of the signals make the systems represented in Figure 1 a particularly valuable test case. Moreover, the available energy range for the UV-visible optical and chiroptical spectra spans several dozens of electronic states, representing a challenging task in terms of computational cost, and in the setup of reliable methodologies.

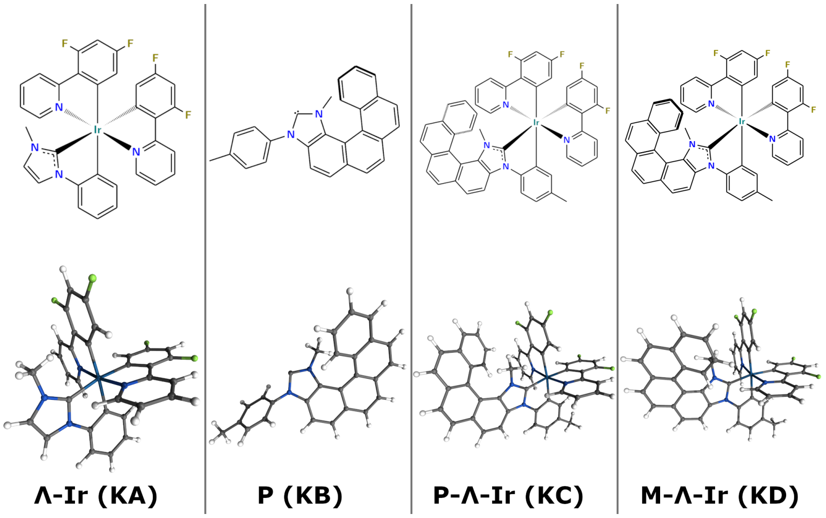

Λ-Ir (KA) **P (KB)** **P-Λ-Ir (KC)** **M-Λ-Ir (KD)**

Figure 1: 2D and 3D representations of the KA, KB, KC and KD molecular systems.

The article is organized as follows. In the first section the theoretical background is presented, the main concepts used for the analysis of the results are recalled and summarized. Particular attention is devoted to the computational strategies, underlining the strengths and the shortcomings of each of the available models. After summarizing the essential computational details, an effective computational protocol is proposed and validated for the parent KA complex and then extended to the larger KC and KD derivatives. Finally, the last section is devoted to conclusions and perspectives for future work.

2. Theoretical backgrounds

The focus of this section is the analysis of the main practical aspects involved in the simulation of vibrationally-resolved electronic spectra, whereas interested readers can find elsewhere details about the theoretical background [**? ? ? ? ? ?**] and on complementary aspects [**? ?**]. Without loss of generality, the discussion will be centered on absorption spectra, whose simulation always starts from the equilibrium geometries of the ground electronic states, obtained through geometry optimization steps. Extension to emission spectra is straightforward and essentially equivalent for the most refined models, but more computationally demanding for less complete approaches due to the inherently greater effort needed to optimize the geometry and compute the harmonic force fields of excited electronic states with respect to ground ones. For instance, in the simplest, vertical excitation model, only the electronic transition moments of the properties of interest, here the electric dipole and magnetic dipole, are needed, which can be obtained from excited-states single point calculations. The resulting stick spectrum is then broadened by means of phenomenological distribution functions to match the recorded one, with part of the broadening accounting empirically for the neglected effect of molecular vibrations. More refined models, properly accounting for most the components of the overall molecular state (rotational-vibrational-electronic or rovibronic,[**? ?**] or vibrational-electronic also known as vibronic[**?**]) can be applied only to small systems, containing at most 2–3 atoms for the most complete one, and less than ten atoms for the second one, despite recent works to speed up the latter.[**?**] A more feasible approach relies on a series of approximations, namely the separation of the electronic and nuclear wave functions, through the Born–Oppenheimer approximation, and then a separation of the vibrational and rotational components of the nuclear motions, using a specific orientation of the molecule in the reference frame to meet the Eckart-Sayvetz conditions. It should be noted that the latter simplification is exact for rigid molecular systems and represents a good approximation for semi-rigid ones, in which the structural changes induced by the electronic transition are small. For the medium-large systems of interest here, the rotational structure does not play a visible role and can be ignored, so that the recorded experimental spectra can be assimilated to an ensemble of transitions between vibrational states belonging to different electronic states, hence the term of vibrationally-resolved electronic spectra, referred to, in the following, as vibronic spectra in a broad sense. Further line broadening and shifting is due to solvent effects, with direct interactions in the cybotactic region (mainly for hydrogen bonding solvents) being usually distinguished from bulk solvent effects. The first contribution can be taken into account by considering a supermolecule formed by the solute plus a reduced number of solvent molecules. Of course, the main difficulty of this approach is the definition of the number and position of solvent molecules to add to the treatment, without increasing too much the overall computational cost. Bulk solvent effects can be effectively represented through polarizable continuum models (PCMs), with additional refinements being employed to account for the broadening induced by dynamical processes.[**?**] The dichloromethane solvent used in the experimental studies of the molecules of interest in the present work,[**?**] can be effectively described with PCM, and the associated broadening will be reproduced empirically by choosing suitable half-widths at half-maxima for the broadening functions to match the experimental band-shape.

Let us now focus on the calculation of the vibronic transitions, considering that an overall UV-visible spectrum is a sum of such transitions. As mentioned above, we actually need to compute transition integrals between the vibrational states of different electronic states, starting from the knowledge of the vibrational energy levels and the associated eigenstates. At the harmonic level, all the necessary information can be obtained through standard force constants/frequency calculations. In comparison with the VE model, it is now necessary to carry out such calculation in the ground electronic state. In addition, the most complete approach, hereafter referred to as adiabatic Hessian (AH) model requires also the equilibrium geometry and the harmonic force field of the excited states. While this model provides all the ingredients to compute vibrationally resolved spectra, its accuracy deteriorates with the distance between the equilibrium geometries of the initial and final electronic state. Indeed, the most probable transitions, and, in turn, the most intense features of a spectral band-shape, will occur for final states overlapping with the initial ones. The harmonic approximation provides a reasonable description of the actual potential energy surface (PES) about its minimum, but quickly diverges with the distance. Thus, if the structural changes become important, the AH model will gradually reduce its ability to represent accurately the region of the final-state PES, which corresponds to the maximum of the transition probability. An alternative approach, hereafter referred to as vertical Hessian (VH) model, has been proposed, which focuses on this region, by computing the final-state energy derivatives at the initial-state geometry, thus avoiding the geometry optimization for the excited state. This model has been shown to improve the computed spectra for molecules exhibiting a non-negligible degree of flexibility,[**?**] at the price of an approximation of the true final-state minimum. Recent improvements have made available analytic second energy derivatives also for excited states, in particular for the time-dependent density functional theory (TD-DFT),[**?** **?**] making this step more computationally accessible. Further simplifications have been proposed to avoid this step at all, by assuming that the electronic transition has a negligible impact also on the vibrational structure, so that the final-state frequencies and normal modes can be assumed equal to their initial-state counterparts. For adiabatic models this means that only the

Quantity	**VE**	**AH**	**AS**	**VH**	**VG**	**FC**	**HT**
Initial state							
Equilibrium geometry	×	×	×	×	×		
Electronic energy	×	×	×	×	×		
Force constants		×	×	×	×		
Final state							
Equilibrium geometry		×	×				
Electronic energy	×	×	×	×	×		
Energy gradients				×	×		
Force constants		×		×			
Transition moments							
Transition moment	×					×	
First derivative							×

Table 1: Quantities requested for each level of calculation to simulate electronic spectra.

excited-state equilibrium geometry must be computed, through an optimization step. Since this approach provides an accurate description of the shift between the equilibrium geometries of initial and final states, this is referred to as adiabatic shift (AS) model. For vertical approaches, the gradient is still needed to extrapolate the equilibrium geometry shift, hence the name of vertical gradient (VG) chosen here. This model is also known in the literature as linear coupling model (LCM[**?**]) or independent-mode displaced harmonic oscillator approximation (IMDHO[**?**]). A summary of the necessary steps to compute the quantities of interest for the different models is given in Table 1, and indicative times needed to generate the different contributions are sketched in Figure 2.

Similar problems are encountered for the electronic transition moments (ETMs) of the properties involved in the different spectroscopic techniques, namely the electric and magnetic dipoles in the present context, since their dependence on the nuclear coordinates is unknown. A standard approximation, proposed by Franck,[**?**] is to consider these quantities constant, owing to the fast motions

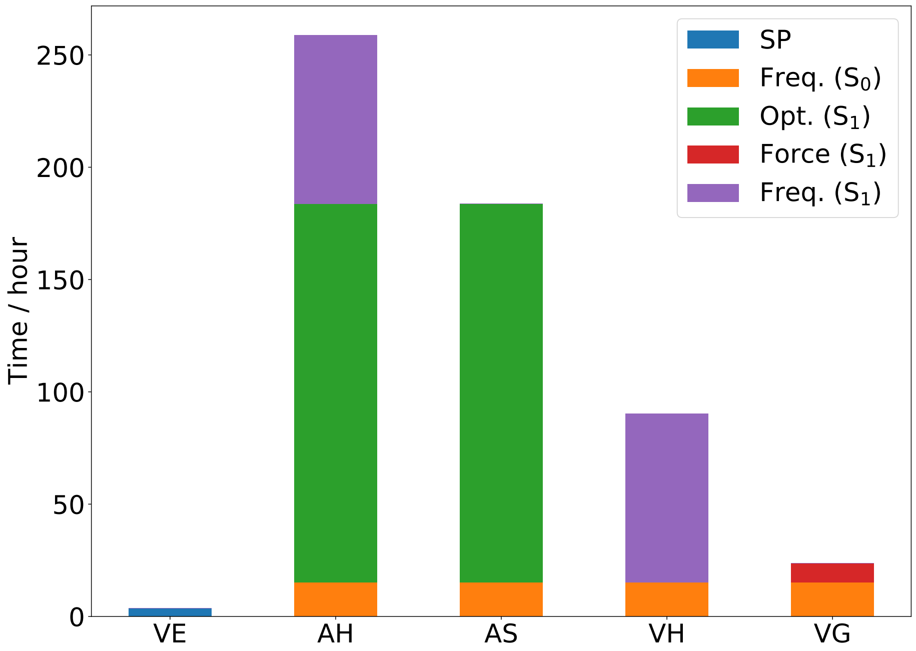

Figure 2: Computational cost of each step for the discussed models. All calculations were carried out on 16 cores (2 processors Intel Xeon E5-2667v2 at 3.3 GHz) with 128 GB of RAM. 6 exited states were included in all TD-DFT calculations. Note that the cost of the optimization step, which was done starting from the S_0 equilibrium geometry, does not depend only on the system size, but also on its flexibility and the quality of the geometry optimizer. To reach a satisfactory convergence, an initial frequency calculation in S_1 at the equilibrium geometry of S_0 was done to ensure that the convergence proceeded correctly.

of the electrons compared to the nuclei. This hypothesis was later formalized in a quantum mechanical framework by Condon,[**?**] so that the hypothesis of constant electronic transition moments in the calculation of transition integrals between vibrational states belonging to different electronic states is known as the Franck–Condon (FC) approximation. This simplification makes the calculations of vibronic integrals simpler, but notably fails in two conditions; first, when the ETM is small, which may happen for dipole-forbidden transitions and, second, when the scalar product of two quantities is close to zero, which can be commonly observed in chiroptical spectroscopies, where the electric and magnetic dipole moments can be nearly perpendicular to one another. An improved description was provided by Herzberg and Teller,[**?**] who considered a linear dependence of the transition moments on the nuclear positions. By including the first derivatives of the electronic transition moment with respect to the nuclear coordinates, the influence of closely lying electronic states can be partially captured, resulting in a more complete picture, which is referred to as the Herzberg–Teller (HT) approximation. The full description of the ETM, including both the constant term (0th order) and the first derivative (1st order) is known either as HT or FCHT (Franck–Condon Herzberg–Teller) level. This latter acronym will be used in the following in order to avoid any risk of misinterpretation in the definition of the model used to describe vibronic transitions. For conventional spectra, the HT contributions are significant only for dipole-forbidden or weakly-allowed transitions,[**?**], whereas the FC approximation is sufficient in other cases. On the other hand, since the ETMs are constant, chiroptical spectra simulated at the FC level are mono-signated, whereas sign alternations can be observed at the FCHT level.

When dealing with medium-to-large molecules or complexes, low-frequency modes can be present, with structural changes induced by electronic transitions along these motions being often quite high. This may result in a breakdown of the theoretical models employed to compute vibrationally-resolved electronic spectra. However, because of their low energy and large shift, significant overlaps with the initial states are possible only for high overtones of these modes, so that the corresponding transitions have almost systematically very low intensity. Such observation applies also to combination bands involving these modes. As a consequence, their contribution to the band-shape will be an overall broadening of all the features and can be assimilated to a background noise, possibly overestimated by the underlying approximations of the theoretical models described above. Based on these considerations, a good approximation would be to use a model system where precisely these low-frequencies (governing to large-amplitude motions) are removed. We can thus devise a two-step strategy consisting in, (i) identifying the vibrational modes to be removed, and (ii) removing consistently the relevant modes in both initial and final electronic states. A simple solution to address the first point is to consider the structural difference between the energy minima in terms of the normal coordinates ($\boldsymbol{Q}$), which describe the vibrational motions of the system, weighted by their energy, and identify all those contributions with a magnitude exceeding a given threshold. This procedure normally uses a single state as reference state one. Even if done on both states, a "reconciliation" operation is necessary to ensure that the system remains consistent upon the transition. In practice, this means that the number of normal modes must remain the same, and that the modes discarded in a state do not appear in the second. This can be mathematically formalized by considering that the total ensemble of normal modes of the system in one state can be expressed in the basis set of the other. The simplest form is to consider an affine transformation,[**?**]

$$\boldsymbol{Q}_I = \mathbf{J}\,\boldsymbol{Q}_F + \boldsymbol{K}$$

where $\mathbf{J}$ is called the Duschinsky matrix, and $\boldsymbol{K}$ the shift vector. The subscript I and F refer to the initial and final states, respectively. Incidentally, the elements K_i can be used for the selection process, or alternatively the dimensionless quantity $K_i\sqrt{\hbar/2\pi c\omega_i}$, where ω_i is the wavenumber (in cm^{-1}) of mode i. In order to ensure the consistency of the model system, the modes to be removed in one state should have no overlap with the modes to be kept in the other, which mathematically translates into the corresponding matrix element of $\mathbf{J}$ being null. The choice of the coordinates becomes critical, as an unsuitable set could inflate the mixing of the modes upon the electronic transitions. This would result in the impossibility of discarding properly large-amplitude motions without having to select a large number of well-described ones since the Duschinsky matrix $\mathbf{J}$ would contain a lot of non-null off-diagonal terms, with the consequence that the model system would bear no resemblance with the actual system. Internal coordinates are known to be able to localize well normal modes, but their definition is not unequivocal. As a result, particular attention needs to be paid to their construction, otherwise the outcome may be even worse than with the more conventional Cartesian coordinates. As a matter of fact, internal coordinates have been often ignored because of the tedious manual process of defining a proper set of coordinates, which becomes impractical with large systems. Over the recent years, automated procedures have started to emerge to greatly facilitate this step, leading to a renewed interest in the use of internal coordinates in vibronic calculations.[? ? ?] Here, we will use the generalized internal coordinates (GICs) implemented in GAUSSIAN, which extend the standard sets of primitive internal coordinates (PICs) built from bonds, angles and dihedral angles with special coordinates like ring puckering or linear angles, and allow their combination, giving the possibility to build coordinates matching the most important structural deformation motions and vibrations. While these coordinates can greatly reduce the mode mixing mentioned above, the real Duschinsky matrix has rarely a perfect block structure, and it is not possible to define minimal sets of normal modes to discard perfectly uncoupled from the rest of the modes. As a result, a tolerance threshold is set to define which amount of coupling will be lost in building the model system. In more technical terms, for a given mode i to be removed, the elements of $\mathbf{J}$ on the corresponding row or column are squared and sorted decreasingly. The first m elements with a total overlap (sum of the associated squared elements) above the threshold are selected to be removed. An iterative process ensure that the sets of modes to be removed in each state are consistent and sufficiently uncoupled from the rest.

3. Computational details

Methods rooted in the density functional theory (DFT)[?] for ground electronic states, and its time-dependent extension (TD-DFT)[? ? ?] for excited states were employed in all the computations. An ultrafine grid (99 radial shells and 590 angular points per shell) was used to integrate the exchange-correlation kernel. Grimme's empirical dispersion corrections[?] were used, in conjunction with the Becke-Johnson (BJ)[?] damping where available. Bulk solvent effects have been taken into account by means of the polarizable continuum model[?

] within its integral equation formalism (IEF-PCM)[**?**], with the cavity build around the solute by means of a combination of interlocking spheres centered on each atom with a radius equal to its van der Waals radius scaled by a factor of 1.1. Values of $\epsilon = 8.93$ and $\epsilon_\infty = 2.03$ were used for the static and dynamic dielectric constants of dichloromethane. In all cases, the non-equilibrium solvent regime was enforced for computing VE's and energy gradients, the latter being computed by the linear response (LR-PCM/TD-DFT) approach[**?** **?**]. These conditions are the most suitable for computing absorption spectra in solution due to the different time scales of the electronic and nuclear motions. Equilibrium structures were obtained using tight convergence criteria (maximum forces and displacements smaller than 1.5×10^{-5} Hartree/Bohr and 6×10^{-5} Å, respectively) for the geometry optimization of the ground and excited electronic states, with the nature of the stationary points being confirmed by Hessian evaluations. 27 combinations of electronic structure calculation methods (ESCM) and basis sets were analyzed to define the most suitable candidate for this system. They include five density functionals, namely B3PW91,[**?** **?**] PBE0,[**?**] LC-ωHPBE,[**?**] MN15,[**?**] and M06-2X[**?** **?**]. Each of them was tested in conjunction with three different basis sets, namely SNSD (an extension of the Pople basis sets 6-31+G(d), which has been extensively validated for both ground and excited states[**?** **?** **?**]) together with double-zeta (pc-1) and triple-zeta (pc-2) polarization consistent basis sets.[**?** **?**] The 6-31+G(d,p) basis set was also tested with the density functional selected in the previous step.[**?** **?**] Both double and triple-ζ basis sets were employed in conjunction with the corresponding LANL and SDD pseudopotential for the Ir atom.[**?** **?**] 50 excited electronic states were included in the benchmark study on KA, and half-widths at half-maximum (HWHM) of 1200 cm^{-1} were used to simulate the natural broadening observed experimentally.

The electronic transition current densities (ETCDs) were computed with a locally modified version of the Cubegen utility of Gaussian and saved as a discretized volumetric dataset in plain-text cube files. 3D ETCD figures representing the vector field were obtained as described in Refs. [**?** **?**]. Space partitioning within the Quantum theory of atoms in molecules (QTAIM) was done with the MULTIWFN package[?] and volumetric datasets were processed with in-house Python scripts.

Vibronic calculations were performed by initially employing the sum-over-states, or time-independent (TI), approach, which computes the total band-shape as the sum of all transitions connecting the manifold of initial and final vibrational states. For this reason, identifying the most intense transitions contributing primarily to the band-shape is straightforward. Conversely, if significant structural deformations are associated to the electronic transition, the large number of small, but non-negligible transitions to take into account makes the convergence of the band-shape very difficult within a reasonable computational time. The *class*-based protocol, extensively described in Refs. [? ? ? ? ?] was used, with the following parameters, $C_1^{\max} = 100$, $C_2^{\max} = 80$, $I^{\max} = 4 \times 10^8$, and combination bands up to 7 simultaneously excited modes in the final states were considered. In order to reach a sufficient progression (above 70%, in most cases, 90%), the generalized internal coordinates available in GAUSSIAN were used. Special coordinates were used, and are reported in Section 3.1 in the Supplementary material. This choice of coordinates helps localizing the normal modes, reducing the contribution of combination bands and the overall noise generated by low-intensity transitions, which cause an artificial broadening of the band-shape. Finally, a reduced-dimensionality scheme was used to remove the contributions from hindered-rotors and large amplitude motions, which did not contribute to the spectral features, but were improperly handled at the Franck-Condon level. For the VG model, an additional issue lies in the extrapolation used to compute the shift vector, which leads to significant overestimations for low-energy modes. Hence, following standard protocols, all modes below 150 cm^{-1} were excluded. For the AH model, the strongly shifted modes – first 20 for KA, first 7 for KC and KD – were excluded. Because the computational cost of TI vibronic calculations grows exponentially with the number of vibrational states, the approach is ill-suited to handle temperature effects for large systems. An alternative route is offered by the path integral or time-dependent (TD) formulation, which allows an automatic inclusion of all initial and final vibrational states, at the expense of the possibility to assign the transitions to the observed bands. All the spectra at 298 K were simulated employing the TD approach, using the default parameters in GAUSSIAN, that is a total time of 10^{-10} s divided in 2^{18} steps for the computation of the autocorrelation function, which leads to the final spectrum.[**?**]

Concerning solvent effects, the state-specific (SS-PCM/TD-DFT) model was chosen for excited states calculations necessary for the AH approach, whereas the linear-response (LR-PCM/TD-DFT) model within a non-equilibrium regime was applied for generating the data needed by the VG model.

Both the Franck–Condon approximation (FC) and its Herzberg–Teller (FCHT) extension were used for the representation of the electronic transition moments of the properties of interest, namely the electric and magnetic dipoles.

Mixed vibronic-electronic spectra were obtained by either convoluting the stick specta over the same discretized X axis (TI), or by interpolating the TD spectra over a new grid, used to convolute the electronic transitions. Gaussian distribution functions were used to simulate the experimental broadening of the bands, with HWHMs of 1200 cm^{-1} for VE and 1000 cm^{-1} for all vibronic calculations, with the reduced value employed in the latter case being related to the explicit account of the vibrational structure.

GAUSSIAN16 was used for the optimization,[**?**] frequencies and single point calculations, and its development version[**?**] for vibronic and related tasks.

4. Results and Discussions

4.1. Benchmark

In the case of medium-to-large systems, DFT remains the method of choice for the simulation of chiroptical spectra. However, the large number of existing functionals, often developed for specific purposes, creates a conundrum in the definition of a suitable computational protocol. This difficulty is partially alleviated by the availability of benchmark studies for a wide range of systems,

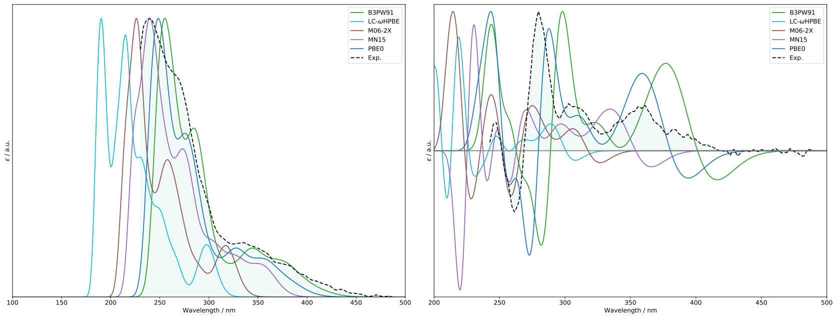

Figure 3: One-photon absorption (OPA, left panel) and electronic circular dichroism (ECD, right panel) spectra of KA computed with different functionals. The broadening was simulated by means of Gaussian functions with half-widths at half-maximum of 1200 cm^{-1}. Each spectrum is normalized to the highest peak.[basis sets: LANL2DZ/SNSD].

which can provide either direct solutions (if similar systems, properties and/or functional/basis set have been already considered) or help in identifying the most suitable candidates for an *ad hoc* test.

In the present study, five popular functionals were chosen, in conjunction with several combinations of pseudo-potentials for the metal atom and basis sets. The total number of combinations still represent a challenge for the systems of interest, KC and KD, so the smaller, model system KA was initially used, where the local environment of the metal center is similar (see Figure 1 for the molecular structure). The full list of different computational setups is reported in Table S1 of the Supplementary material, and the transition energies and intensities for the first five electronic excitation are given in Table S2.

In a first step, only the exchange-correlation functional was modified, using always the same the pseudo-potential and basis set (LANL2DZ and SNSD, respectively). Figure 3 shows the impact of the functional on the band-shape in the 230-480 nm wavelength range, which includes the first 50 excited electronic states. The analysis of the one-photon absorption (OPA) spectra allows a first screening of the methods to be further refined with reference to the electronic circular dichroism (ECD) experimental spectrum. As shown in the left panel of Figure 3, the MN15 functional shows the smallest energy shift with respect to experiment. However, in spite of a slight underestimation of the transition energies, PBE0 and B3PW91 produce an overall spectral band-shape in fair agreement with experiment. Turning now our attention to the chiral spectroscopy, MN15 results in a spectrum sensibly worse than PBE0 and B3PW91. Between the latter two functionals, B3PW91 reproduces better the relative positions of the bands within the spectrum, and was therefore selected for the further tuning of the basis in the quest for the best computational protocol.

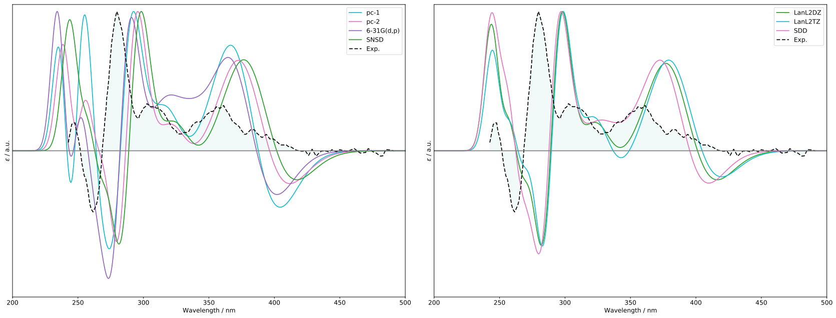

Figure 4: Effects of different basis sets (left panel) and pseudo-potential (right panel) on the ECD spectrum of KA. The broadening was simulated by means of Gaussian functions with half-widths at half-maximum of 1200 cm^{-1} (OPA results are reported in Figure S1 in Supplementary material).

Since the disagreement among the different electronic structure methods are larger for chiroptical spectroscopic techniques, the ECD spectrum has been used for further validations. In the left panel of Figure 4, the simulated spectra obtained with the B3PW91 functional and different basis sets are reported. Two basis sets were studied in this connection, namely the pc-1 and pc-2 double- and triple-ζ basis sets, proposed by Jensen and collaborators as optimized versions of Dunning's basis sets for DFT computations.[**?**] The pc-1 basis set overestimates the relative intensity of the first experimental band at 360 nm, with a strong negative band at a lower energy, not visible in the experimental spectrum. The experimental band at about 310 nm is almost fused to the highest-intensity band, becoming a shoulder. The larger basis set improves the results, lowering the relative intensity of the bands above 300 nm. The shape of the band at 310 nm is also better defined, exhibiting a clearer feature, which remains, however, slightly too close to the neighbour band. The augmented Pople's basis set, SNSD gives very comparable results with significantly reduced computational cost. Removing the diffuse functions (6-31G(d,p)) leads to a decrease of the band intensities in the 340–450 nm region. While this makes the band at 360 nm closer to experiment in terms of relative intensity, an excessive broadening is obtained, leading to a merging with the band immediately before in terms of wavelengths. It is noteworthy that, because of the symmetric convolution used, the broadening is often underestimated, especially concerning the strongly asymmetric vibrational contributions. Consequently, the explicit inclusion of vibronic effects generally lead to lower intensities. Based on these observations, the SNSD basis set represents the best compromise between cost and accuracy and will be used as reference in the following. The effects of the pseudo-potential and the size of the basis set on the metal atom were are shown in the right panel of Figure 4. Changing from LANL2DZ to SDD worsens the agreement with experiment, while increasing the basis set size from double-ζ (LANL2DZ) to triple-ζ (LANL2TZ) improves the results only marginally, while increasing significantly the computational cost.

Thus, considering both accuracy and computational cost, the B3PW91/LANL2DZ/SNSD combination was chosen as the most suitable level of theory for the systems under investigation.

4.2. Vibronic Simulation

As shown in Figure 5, after a careful selection of the computational method, a purely electronic approach is already capable of reproducing satisfactorily the OPA spectrum of KA. On the other hand, for the more sensitive chiroptical spectroscopy, stronger discrepancies appear with respect to the experimental spectrum. In particular, in the ECD spectrum, the first band shows, contrary to the experiment, a negative sign, and the height of the second band (first experimental band) is significantly overestimated.

In order to improve the computational results, a first step is to include vibra-

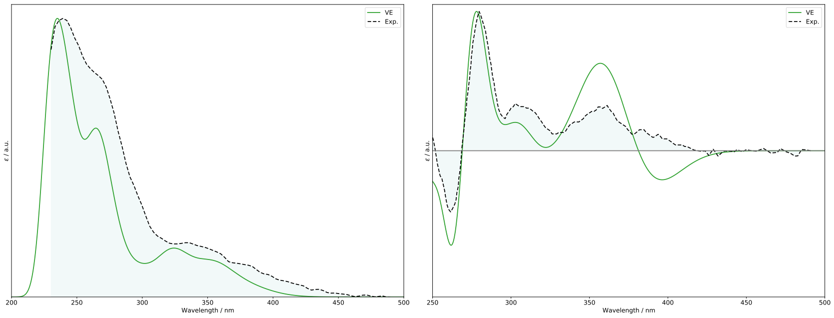

Figure 5: Pure electronic (VE) one-photon absorption (OPA, left panel) and electronic circular dichroism (ECD, right panel) at the B3PW91/LANL2DZ/SND level of theory. The broadening was simulated by means of Gaussian functions with half-widths at half-maximum of 1200 cm^{-1}.

tional modulation effects, which can play a fundamental role in the low-energy region of the spectra, which are characterized by a low density of electronic transitions. In the following sections, the computational protocol to simulate the vibronic spectra will be optimized for the prototype KA molecule, and then extended to KC and KD.

4.2.1. Modelling the first electronic transition of KA

The $S_1 \leftarrow S_0$ electronic transition is mainly a HOMO to LUMO transition with a metal-to-ligand charge transfer character, as confirmed by the analysis of the electron density difference (see Table S3 and Figure S2 in Supplementary material). The charge is concentrated on the pyridine rings of the phenylpyridine ligands. Therefore, assuming that the disagreement between the spectra computed at the VE level and experiments is due to the lack of vibronic contributions, we started by fully characterizing the S_1 excited state and simulating the vibronic spectra within the AH approach (AH|FC). The dependence of the electronic transition moments on the nuclear positions was also taken into account (AH|FCHT), since it can lead to sign changes in the vibronic spectra. When dealing with large, semi-rigid systems, large amplitude motions (LAMs) and mode mixing are important aspects that need to be evaluated. The comparison of the equilibrium geometries of the ground and first excited electronic states (reported in Figure S3 in Supplementary material) reveals a general distortion of the coordination geometry with a shortening of the Ir$\cdots$Py and Ir$\cdots$NHC bonds and an elongation of the Ir$-$C bonds. These type of deformations, which involve the relative positions of several atoms are often poorly described by Cartesian coordinates, leading to over estimation of the mode mixing. Starting from the set of GICs generated automatically by the GAUSSIAN program, an *ad hoc* set of internal coordinates were added in order to represent the relative orientations of the ligands around the metal center, with the aim of improving the description of the transformation associated to the low-energy normal modes. This allows localizing the normal modes, reducing in this way the coupling between them, as well as recovering some of the intrinsic anharmonicity of the vibrational motions.

The lower mode mixing from the use of internal coordinates is apparent on inspection of the **J** matrices obtained with rectilinear or curvilinear coordinates (left half of Figure 6). Indeed, **J** is slightly more diagonal and, especially, the coupling between low- and high-frequency modes is strongly lowered. In order to evaluate better the effects of the couplings on the band-shape, the so-called Sharp–Rosenstock **C**[**?**] matrices, which are directly related to the intensity of the combination bands,[**?** **?** **?**] are reported in the right panels of Figure 6. The use of GICs substantially reduces the overlap between modes of low- and high-energy (it should be noted, that one order of magnitude difference exists between the two normalizing factors of **C** matrix representations), which can contribute to an artificial broadening of the bands.[**?**] This also makes easier the isolation and removal of the large amplitude motions. By doing so, it is possible to recover 91% of the total intensity in TI vibronic simulations, from the initial value of 30% for the reduced system in Cartesian coordinates.

The AH and experimental spectra are compared in Figure 7. Both AH|FC and AH|FCHT models lead to a red-shift and an intensity reduction of the bands in comparison to the VE results. While the sign remains negative, this result appears qualitatively consistent with experiment, which does no show any prominent band in this region of whatever sign. The stick spectrum, displayed

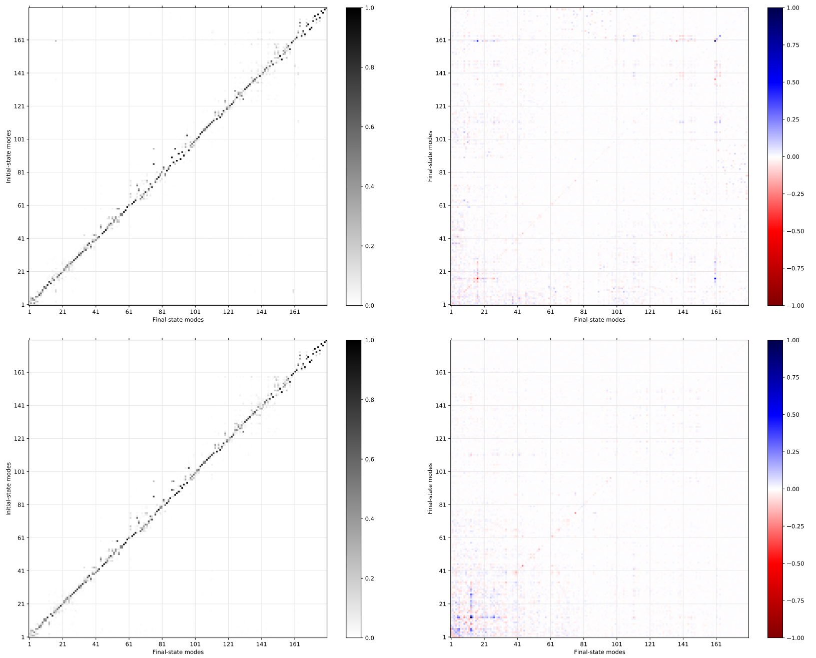

Figure 6: In the top panels, the **J** and **C** matrices (normalization factor: 7.33e-01) obtained in Cartesian coordinates, and in the lower panels, those obtained with GICs (normalization factor: 7.50e-02). The normalization factor is based on the highest absolute element of each **C** matrix. Each element of the Duschinsky matrix is squared and a shade of gray is applied to it (0: white, 1: black).

in Figure 7 as well, shows a non-negligible impact of the HT effects on the final band-shape, with many low-intensity positive transitions partially compensating the intense negative peaks. This causes a flattening of the FCHT band compared to the FC counterpart, accompanied by a slight shift of the maximum. As can be inferred from Figure 5, and will be discussed in more details below, this band can be compensated by the higher-energy transitions, resulting in a better overall agreement with experiment.

The analysis of the vibronic contributions to the ECD spectra is limited due to the low resolution of the experimental spectrum. Nonetheless, here we report the most significant contributions to the first band. For both AH|FC and AH|FCHT models, three vibrational modes, $\overline{\overline{28}}$, $\overline{\overline{33}}$ and $\overline{\overline{156}}$, together with their

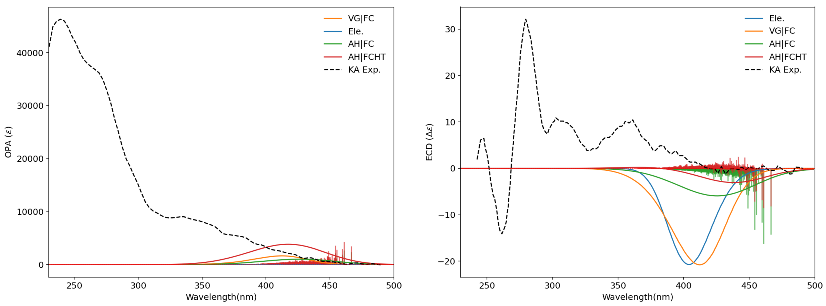

Figure 7: $S_1 \leftarrow S_0$ OPA and ECD spectra of KA. The vibronic results (AH and VG) are compared to both VE and experiment. The broadening was simulated by mean of Gaussian distribution functions with half-widths at half-maximum of 1000 cm^{-1} for vibronic and 1200 cm^{-1} for VE calculations.

overtones and combination bands, represent 90% of the most intense transitions. Indeed, the most prominent contributions are ascribed to the fundamentals of modes $\overline{\overline{28}}$ and $\overline{\overline{33}}$, which are more intense than the 0-0, transition between the vibrational ground states. These modes, depicted in Figure 8, involve the concerted oscillation of several atoms spread over the whole molecule, making their classification difficult. Nonetheless, all of them are predominantly localized on the two 2-(2,4-difluorophenyl)-pyridyl (dfppy) ligands, in line with the geometric rearrangements and the difference in electron density reported in Figures S2 and S3 in Supplementary material, with this finding underlining once more the necessity of a good set of coordinates for the proper description of the coordination sphere.

4.2.2. Overall vibronic spectra of KA

The simulation of higher-energy states at the AH level is conditioned by the optimization process, which can become extremely challenging.[**?**] Furthermore, as the density of states grows in the energy range of interest, the most important aspect becomes the reproduction of the most intense bands, which are connected to the region of high overlap with the ground electronic state. For this reason, vertical models are generally more suitable to treat spectra involving several highly-excited electronic states. The VH model is the most ac-

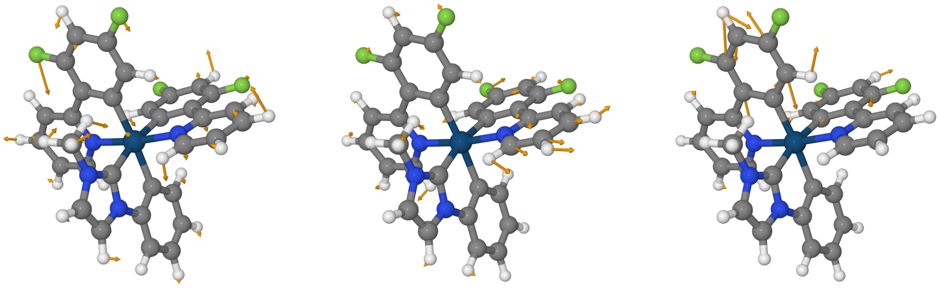

$\overline{\overline{28}}$ $\overline{\overline{33}}$ $\overline{\overline{156}}$

Figure 8: Representation of the most relevant normal modes related to the vibronic contributions.

curate, but it requires frequency calculations for each electronic state, which can make the computations very expensive. Moreover, it is significantly dependent on the anharmonicity of the final-state PES and the vicinity of intersections, which can cause a breakdown of the adiabatic picture. In the present case, as shown in Figure S4 in Supplementary material, the VH|FC model does not represent an improvement with respect to the simpler VG|FC approach, whereas the VH|FCHT model shows an unphysical behavior, which prevents its use. In conclusion, the VG model offers the best compromise between accuracy and feasibility, [**? ? ? ?**] and has been selected for the next part of our study.

Considering the density of the electronic states, vibronic contributions need to be computed for the first 23 transitions of the systems under investigation, making problematic the systematic use of diffuse functions for the gradient evaluation of such a large number of different electronic states, especially for the large KC and KD systems. For this reason, the reliability of smaller basis sets for excited-state gradients needs to be assessed. In the present work, the following strategy was devised. All the calculations for the ground electronic states were performed with the larger basis set, with the corresponding equilibrium geometry being used as reference. The transition dipole moments and excitation energies, which require single-point calculations and are necessary for the VE spectra, were obtained at this level as well. Then, the forces were computed at a lower-level and compared with their higher-level counterparts. As a matter of fact, the gradients obtained for 12 electronic states with a lower-level computational model employing the LANL2DZ setup for Ir and the 6-31G(d,p) basis set for all the other atoms are in remarkable agreement with higher-level counterparts (see Figure 9).

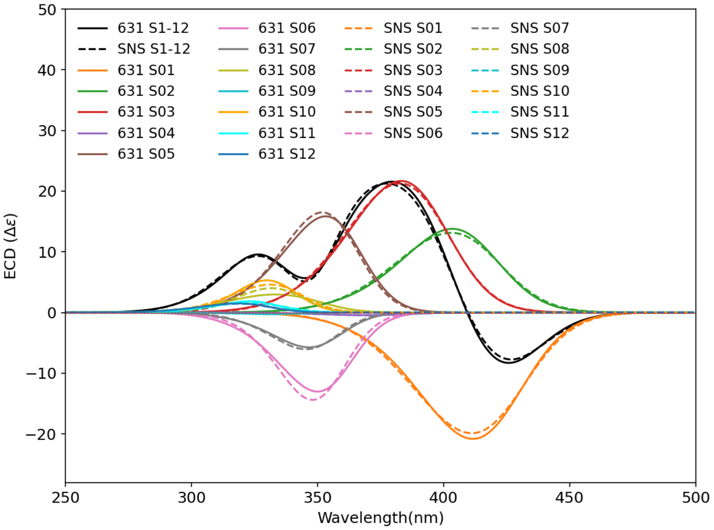

Figure 9: Comparison of the $S_n \leftarrow S_0$ ECD spectra of KA at the VG|FC level with n=1 to 12. The B3PW91/LANL2DZ/SNSD (dashed lines, labelled SNS) and B3PW91/LANL2DZ/6-31G(d,p) (solid lines, labelled 631) levels of theory were used for the force calculations. All other calculations were carried out at the B3PW91/LANL2DZ/SNSD level (see text for details). The broadening was simulated by mean of Gaussian distribution functions with half-widths at half-maximum of 1000 cm^{-1}.

For nearly all the electronic spectra, the band-shape is characterized by a prominent 0-0 transition, and a pattern of vibrational progressions on the high-energy wing, whose vibronic transitions are related to vibrations involving the relative rotation of the ring of the ligands. A graphical representation of the most relevant normal modes is provided in Figure S5 in Supplementary material.

4.3. Toward larger systems: a combinational approach

The hybrid VG method described above can effectively predict the UV-vis spectra in the lower- to medium-energy region. At higher energy, the density of electronic states becomes huge, thus reducing significantly the visibility of vibronic contributions. Hence, pure electronic spectra can be used at this point. It is thus possible to produce high-quality UV-vis spectra by combining properly vibronic and electronic spectra to maintain the overall computational cost under control. Such a procedure becomes mandatory when larger systems, like KC and KD, are tackled. However, several aspects must be carefully considered in this process. Besides finding the right number of transitions to treat at the vibronic level, the problem of the relative broadening schemes need to carefully assessed. In order to get the most reliable description, the broadening can be chosen initially by fitting the vibronic spectra to experimental data, possibly using some alternative schemes to represent the solvent effects.[**?**] Then, the broadening to be used for the more approximate VE model can be chosen to match the final vibronic spectra. This was done here using the $S_1 \leftarrow S_0$ transition of KA. Gaussian distribution functions with HWHMs of 1200 cm^{-1} and 1000 cm^{-1} were used as broadening functions for pure electronic and vibronic transitions, respectively. These results confirm the initial choices for the pure electronic spectral band-shape.

The final OPA and ECD spectra of KA are shown in Figure 10, with the simulated ones computed at different levels and shifted by -22 nm. The purely electronic spectrum, already reported in Figure 5, is compared to several hybrid vibronic-electronic models. For all of them, transitions from the ground state to S_2 up to S_{23} are treated at the VG|FC level, with the forces computed with the 6-31G(d,p) basis set for the non-metallic atom, as described above. The last 27 transitions (S_{24} to S_{50}) are represented by purely electronic transitions. The difference among the three hybrid models lies in the representation of the first transition, obtained at the AH|FC, AH|FCHT and VG|FC levels. All the spectra were normalized to focus on the band-shape, while the non-normalized spectra are reported in the Supplementary material (Figure S6). For OPA, the overall agreement was qualitatively good already at the purely electronic level, with small but significant changes being introduced by more refined approaches. Inclusion of the vibronic contributions for the first 23 electronic transitions improves the shape o the spectrum above 300 nm, and the visible VE band at about 320 nm becomes a shoulder, in closer agreement with experiment. The differences between AH|FC and AH|FCHT are mild, but the slope of the lower-energy wing is too low for the latter, which is due to an overestimation of the intensity of the first transition, likely related to an excessive influence from the neighbor states. This effect is less obvious in ECD because of the changes in the relative transition dipoles orientation which compensate the gain in intensity. Focusing now on the ECD spectra, the band at 310 nm is more clearly separated from the intense peak at about 280 nm, in line with experiment, but it remains still significantly underestimated in terms of relative intensity. For the first large band between 340 and 420 nm, VG|FC shows a relative intensity closer to the experimental band, compared to both AH and VE. Since the transitions involved in the 340–380 nm region should be at the same level (VG|FC) also for AH,this improvement is due to the counterweight of the large negative band from the first transition. The low-intensity negative band observed in the AH computation is partially compensated by the large positive neighboring band, resulting in a flat region between 410 and 450 nm, without any negative feature, in agreement with experiment. The flatter FCHT band gives a lower contribution at 360 nm, which is thus slightly higher than the FC counterpart. Still both vibronic methods give a significantly less intense first band than VE.

As a result, for the current family of systems, the hybrid vibronic-electronic scheme is very appealing in terms of accuracy, with the transition corresponding to the first electronic state in the vertical region being better described at the AH level. While Herzberg–Teller effects can be sometimes significant, here they are small, due primarily to the large broadening used, which causes a dilution of the small transitions. Moreover, the intensity borrowing highlighted in the OPA spectra suggests that the HT terms should be added with special care in the present context. For these reasons, the hybrid scheme chosen for the larger systems will be AH|FC for the first excited electronic state, VG|FC for the transitions to the successive states covering the first bands (up to about 300 nm), and finally purely electronic transitions for higher energies.

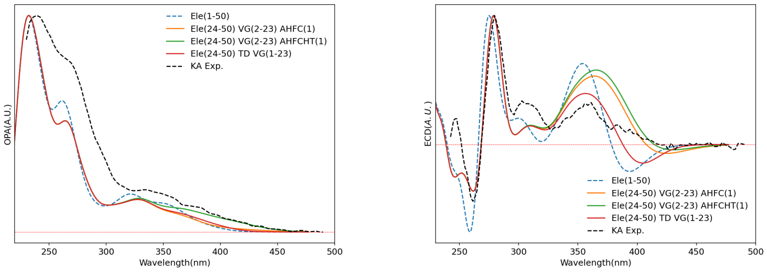

Figure 10: Simulated OPA and ECD spectra of KA, compared to experiment. All the spectra were normalized with respect to the highest band. The purely electronic transitions (VE) were computed at the B3PW91/LANL2DZ/SNSD level, like the data for the vibronic models AH|FC and AH|FCHT. For VG|FC, all the data were computed at the same level, except the energy gradients, generated at the B3PW91/LANL2DZ/6-31G(d,p) level (see text for details). Purely electronic transitions were broadened by means of Gaussian distribution functions with HWHMs=1200 cm^{-1}, while HWHMs of 1000 cm^{-1} were used for the vibronic models.

The protocol developed for KA was applied directly to KC and KD, tuning only the thresholds, i.e., the number of excited states treated at each level. Interestingly, for both KC and KD, a crossing occurs during the optimization step between the first two electronic states, which was not observed for KA. For consistency with KA, the first excited singlet obtained by full geometry optimization was selected, which actually corresponds to S_2 at the ground-state equilibrium geometry, as confirmed by the analysis of the orbital transitions. Using this numbering, the transitions to the first 19 excited states for KC and 18 for KD were computed at the VG|FC level, except for the second one, computed at the AH|FC level. The other transitions up to S_{50} were treated at the VE level. The final hybrid spectra were shifted by -24 nm for KC and -30 nm for KD. The OPA and ECD spectra are reported in Figure 11. In analogy with KA, the spectra were normalized with respect to the most intense experimental band in order to compare the band-shapes, whereas the non-normalized spectra are reported in Figure S7 of the Supplementary material. In the-low energy region (above 350 nm) of the OPA spectrum, vibronic effects reinforce the contribution of the first transitions for both systems, thus providing less steep curves, whose shape resembles more closely the experimental counterpart. For ECD, the purely electronic spectra show already a good qualitative agreement with experiment and, in particular, a reproduction of the right sign pattern between 300 and 450 nm. The impact of the inclusion of vibronic effects is here more subtle, with a slight red-shift of the first-band maximum closer to experiment, but a small overestimation of its intensity for both systems. For KC, vibronic effects smoothen the spectrum profile in the region including the two components of the large positive band between 300 and 380 nm, but at the price of an overestimation of the red-wing intensity. Conversely, in KD, vibronic effects lead to the appearance of two distinct peaks in the 280–320 nm region, in agreement with experiment. The band at 340 nm remains too narrow and intense. In conclusion, the results confirm the importance of vibronic effects for the reliable reproduction of spectral shapes. Higher levels of theory, combined with larger basis sets could potentially improve slightly the results, but with a dramatic increase of the overall computational cost.

These results give us a good level of confidence to tackle the problem of the $T_1 \rightarrow S_0$ phosphorescence spectra of KC and KD. Proper computation of intensities for circularly polarized phosphorescence (CPP) spectra requires additional elements in the definition of the Hamiltonian, with the inclusion of relativistic effects, which are not readily available in standard electronic structure calculations. Several programs have been tested to this end, with only partial success. In particular, the latest revision of the ORCA package[1] cannot provide the sign of the rotatory strength, the standalone ReSpect program[2] failed to produce

---

[1] ORCA 4.2.1 at the time of writing (Dec. 2020), see `https://orcaforum.kofo.mpg.de/viewtopic.php?f=26&t=5336`

[2] ReSpect 5.1.0 at the time of writing (Dec. 2020), see `http://www.respectprogram.org/program.html`

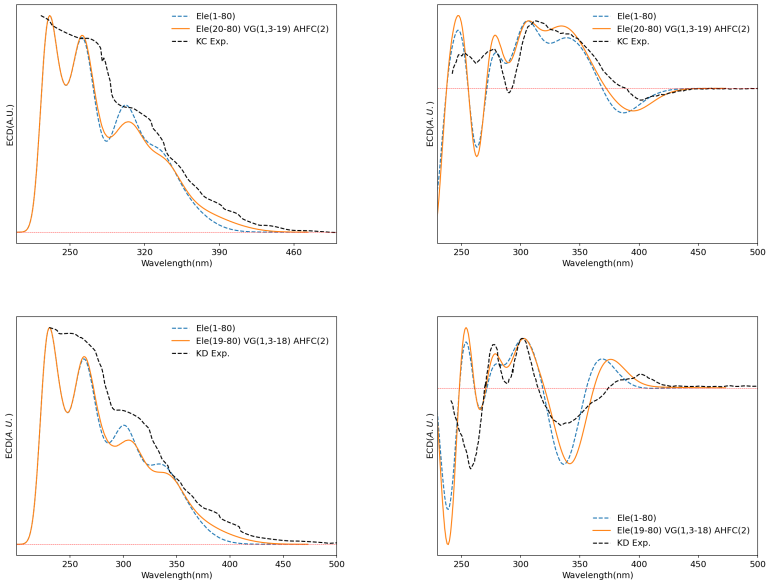

Figure 11: Simulated OPA and ECD spectra of KC (upper panels) and KD (lower panels), compared to experiment. All the spectra were normalized with respect to the highest band. The purely electronic transitions (VE) were computed at the B3PW91/LANL2DZ/SNSD level and the same applies to the vibronic models AH|FC and AH|FCHT. For the VG|FC model, all the data were computed at the same level, with the exception of energy gradients, which were evaluated at the B3PW91/LANL2DZ/6-31G(d,p) level (see text for details). Purely electronic transitions were broadened by means of Gaussian distribution functions with HWHMs=1200 cm^{-1}, while HWHMs of 1000 cm^{-1} were used for the vibronic models.

any usable result and the Dalton program[3] supports only the B3LYP functional for CPP calculations. As a consequence, the quality of B3LYP was first assessed looking at the $S_1 \leftarrow S_0$ transition on the systems of interest to check that it could at least reproduce the sign of the transition. The rotatory strengths for the first transition of KA, KC and KD are given in Table S4 in the Supplementary material. For all the systems, the sign of the ECD spectra are coherent with those computed at the B3PW91 level using GAUSSIAN16, though the rela-

---

[3] Dalton2020 at the time of writing (Dec. 2020), see `https://gitlab.com/dalton/dalton/tree/release/2020`

tive intensities are different. However, for what concerns the CPP spectra, the sign is correctly predicted for KA and KC, but not for KD. Since at the FC level, the transition moments are assumed constant, they act as simple scaling factors of the overall band-shape intensity, so that unitary transition moments can be use instead to evaluate vibronic effects on the band-shape. Let us start with the one-photon phosphorescence (OPP) spectra, which are better resolved experimentally to use as reference. The vibronic AH|FC band-shape is reported in Figure 12, and matches well the experimental results, confirming that the inclusion of vibrational effects is necessary to reach a satisfactory agreement. The two major bands in the spectra are well reproduced both in their position and relative intensity, and the shoulder at 630 nm is present, even if more pronounced in the theoretical spectra. At this level, we see a strong contribution from the 0-0 transition in the first peak with the contribution of modes $\overline{\overline{39}}$ and $\overline{\overline{70}}$, the first being characterized by Ir$\cdots$N stretchings, as well as stretchings and bendings delocalized on all the ligands, while the latter is mostly localized on the two dfppy ligands. However, the most intense peak in the spectrum at ≈565 nm is characterized by the vibronic contributions of modes $\overline{\overline{190}}$ and $\overline{\overline{218}}$, both of them being entirely localized on the helicene fragment of KB ligand (see Figure S8 in SI). These observations confirmed the crucial role played by the helicene in the phosphorescence process as also suggested by the electron density difference between the T_1 and S_0 states (see Figure S9 in Supplementary material). Overall, a number of paths for improving the results can be considered. First, more robust and user-friendly implementations would strongly help the generalization of such calculations. Second, the proper inclusion of Herzberg–Teller effects is not yet possible to the best of our knowledge, even if our code is already able to handle it. Analytic first derivatives have been proposed for the perturbative description of the relativistic effects,[**?**] but they do not seem available in standard quantum chemical packages. Conversely, the variational formulation provides a more robust path, but the derivation is less straightforward, and it has not yet been fully developed. Numerical differentiation is impractical in both cases because of the problem of the phase.

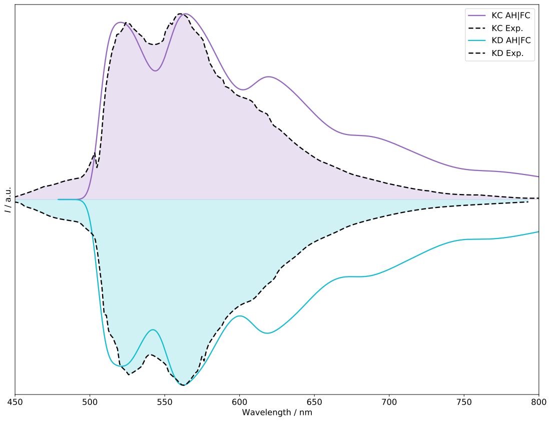

Figure 12: Simulated one photon phosphorescence (OPP) spectra of KC (upper panels) and KD (lower panels), compared to experiment. All the spectra were normalized with respect to the highest band. The purely electronic transitions (VE) were computed at the B3PW91/LANL2DZ/SNSD level and a shift of 22 nm was applied. HWHMs of 200 cm^{-1} were used for the vibronic model.

4.4. At the origin of the iridium complex/helicene interaction: Transition Current Density

As for the parent KA system, the first transition for both KC and KD has mainly a metal-to-ligand character with a major HOMO to LUMO+1 contribution (see Table S3 in the Supplementary material for the description of the transitions in terms of molecular orbitals (MOs) and Figure S2 for a representation of $\Delta\rho$). As previously suggested,[**?**] a strong interaction exists between the π-helical-carbene moiety and the iridium atom. Although minor, the analysis of the frontiers molecular orbitals (see Figure S10 in the Supplementary material) highlights the involvement of the helicene fragment in the transition. Indeed, though similar in their nature (see Figure S2 and Table S3 in the Supplementary material), the rotational strengths of the first transition are quite different. If we compare the rotational strengths (RS) of the unperturbed KA prototype molecule (-62.4$\cdot$10^{-40} esu^{2}cm^2) and the ones of KC and KD, we find that it is almost doubled in KC (-105.5$\cdot$10^{-40} esu^{2}cm^2) and halved in KD (-28.4$\cdot$10^{-40} esu^{2}cm^2) testifying a matching and miss-matching interaction between the two chiral cores of the complexes. With the aim of better investigating the interaction between the two chiral centers within the system, we looked at the electronic transition current density (ETCD).[**?** **?** **?**] ETCD is a vector field, which represents the paths connecting two different probability densities and its integral is associated with the velocity form of the electric dipole transition moments. The visualization of the vector field and the identification of linear and curved patterns in the charge flow occurring upon excitation allows to relate them to the electric and magnetic dipole transition moments, respectively, a possibility recently applied successfully to the investigation of chiral signatures in electronic spectra of medium-large inorganic systems.[**?**] It is worth noting that all the required quantities to compute the ECTD are readily available from the calculation requested for the vibronic calculations, making its computation inexpensive.

In the left panels of Figure 13, the ETCD vector fields of KC and KD are represented by means of "streamtube" objects. For both systems, an intense circulation of charge is observed around the metal center.[**?**] Although less intense than the field surrounding the Ir atom, it is possible to observe linear patterns of charge flowing from the metal atom to the two dfppy ligands, where they cross the conjugated systems. This phenomenon is likely the source of the electric dipole transition moments. In order to highlight the small contributions of the helicene fragment to the ETCD, we attempted to partition the ETCD contribution over different molecular fragments. Since KC and KD are substantially the KA complex where the carbene ligand is replaced by a carbene-helicene ligand, a natural partition scheme would be to separate the KA fragment and the helicene (See Figure S11 in the Supplementary material for a visual representation of the fragments).

As recently proposed by some of us,[**?**] the vector field partition was accomplished by using the quantum theory of atoms in molecules[**?**] to partition the total space, according to the topology of the initial-state electron density, into atomic basins, which were then combined to obtain the subspace of each fragment. In the central panels of Figure 13, "Hedgehog" representations of the

ETCD in which the helicene contribution (depicted in red shades) was magnified by 20 times, are reported. Aside from the prevalent charge flow connecting the metal to the two dfppy ligands (in blue shades), only small regions of circulation of charge are observable on the helicene fragments. In Figures S11 and S12 in the Supplementary material, the contribution of each fragment to the dipole strength (DS) and the RS are represented graphically. Two different partitions were attempted, favoring the KA or KB fragments, respectively. For both system, the major contribution, which determines the sign of the first ECD band is related to the iridium fragment, while the direct impact of the helicene on the RS is marginal, independently of the representation chosen. However, the cross-terms, which represent the couplings of the transition dipole moments localized on different fragments, are non-negligible. For KC, they enhance the strength of the signal, while for KD, they are opposite, resulting in a reduction of the transition intensity.

In order to overcome the problem of visualizing contributions to the vector field with different orders of magnitudes, an alternative representation is used in the right panels of Figure 13. An effective rotatory strength, $\mathbf{R}^m$, is built from the scalar product between the electronic transition moment of the magnetic dipole at each point of a 3D grid and the total electric transition dipole moment, both quantities being computed from the ETCD vector field.[**?** **?**] Integration of this scalar field over all space yields the ECD intensity. This representation shows the spatial dependence of magnetic component of the rotatory strength, with red isosurfaces denoting negative contributions to RS and the blue ones positive contributions. This latter representation clearly depicts the interaction between the two chiral centers in the molecule with the *P* configuration of the helicene which concur to the negative sign of the transition, therefore allowing the emergence of the first negative band in the ECD spectrum of KC. On the other hand, the *M* configuration going in an opposite direction with respect to the contribution of the Λ configuration at the metal sensibly reduces the intensity of the first transition which is therefore hidden by the transitions at higher energy with positive signs. A complementary representation ($\mathbf{R}^\mu$), reported in

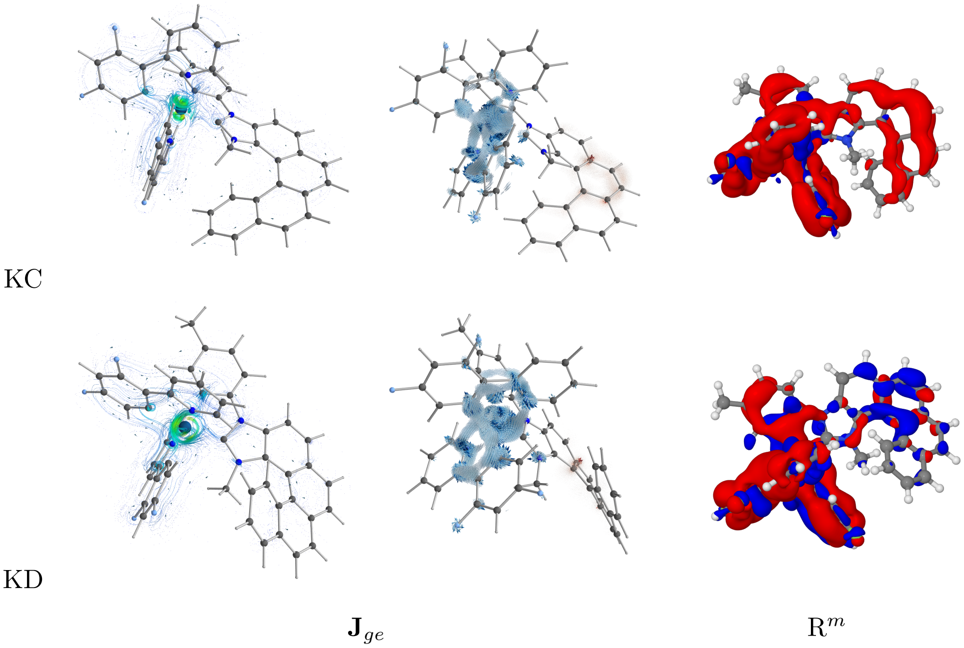

Figure 13: In the left panels, the the ETCD ($\mathbf{J}_{ge}$ vector fields are represented by mean of streamtube objects. In the central panels, the ETCDs have been partitioned between the Ir block and helicene contributions, with the helicene field being magnified 20 times. The resulting fields are displayed using the "Hedgehog" representation. In the right panels, isosurface representations of the point-by-point value of the rotatory strength ($\mathbf{R}^m$ scalar field) are displayed. Red lobes correspond to negative contributions to the rotatory strength, blue for the positive ones.

Supplementary material (Figure S13, can be obtained by projecting the point-by-point transition electric dipole moment on the total magnetic one, which provides information on the spatial dependence of the electronic components of the rotatory strength. Concerning the helicene fragment, the "$\mathbf{R}^\mu$ representation" reveals contributions similar to "$\mathbf{R}^m$", confirming the strong interaction between the helicene-carbene conjugate system and the [Ir(dfppy)$_2$] fragment.

5. Conclusions

Thanks to ongoing efforts in different groups, the route has been paved for the routine computation of vibronic spectra for a growing number of systems of increasing size and complexity. On these grounds, the main aim of this contribution was the presentation and application of novel effective quantum chemical tools going beyond the standard practice of simulating chiroptical spectra by a collection of vertical electronic transitions modulated by phenomenological shape functions.

For purposes of illustration, we have developed and validated a computational protocol for the simulation of OPA and ECD spectra of a family of Ir complexes, starting from the benchmark of density functionals and basis sets for a prototypical molecule to the simulation of the vibronic spectra of more complex systems involving tens of elementary electronic transitions. This protocol paves also the way to the study of chiral and non-chiral phosphorescence spectra, where the band-shape can be closely matched by vibronic calculations.

Concerning vibronic effects, after tuning different parameters in order to achieve a reliable yet effective description of the spectral shapes, we have finally reached the following conclusions: (i) curvilinear coordinates play a crucial role in decoupling the vibrational modes, thus allowing an improved representation of the structural changes induced by electronic transitions. Clever selection of generalized internal coordinates offers thus a clear advantage over customary Cartesian coordinates; (ii) different strategies can be followed in different regions of the spectra according to the density of the transitions and then combined to obtain the final spectrum. Starting from the most refined adiabatic models for well-resolved or isolated bands, one can shift to vertical approaches for reproducing the envelope of more closely-spaced electronic transitions and then to a pure electronic description of the high-energy portion of the spectrum, where the density of the transitions justifies the use of phenomenological band-shape functions. A further reduction of the computational cost can be achieved by a hybrid scheme coupling excited-state gradients computed at a relatively low level of theory with transition energies, transition moments and ground-state force constants computed at a higher level. Purposely tailored graphical representations, like electronic transition current density, which shows the local contributions to the electric and magnetic transition dipole moments, can be profitably used to investigate the interaction between the two chiral centers, identifying the regions giving the largest contributions to the main features and the intensity of the first band.

Even pending further developments in several aspects of the proposed computational strategy (e.g., improved functionals, explicit solute-solvent interactions, more effective treatment of spin-orbit coupling derivatives, automatic definition of internal coordinates) we think that the present study convincingly shows that we already dispose of a quite general, robust and user-friendly tool for accompanying the experimental spectroscopic investigation of large systems of current scientific and technological interest.

6. Acknowledgments

This work has been supported by the MIUR 'PRIN 2017' (Grant Number 2017A4XRCA) and by the Italian Space Agency (ASI; 'Life in Space' project, N. 2019-3-U.0). The SMART@SNS Laboratory (http://smart.sns.it) is acknowledged for providing high-performance computing facilities.

References

[1] J. Franck, E. G. Dymond, Elementary processes of photochemical reactions, Transactions of the Faraday Society 21 (1926) 536–542. `doi:10.1039/TF9262100536`.
URL `http://dx.doi.org/10.1039/TF9262100536`

[2] J. Franck, F. Weigert, H. v. Halban, M. Bodenstein, E. C. C. Baly, B. Lewis, D. L. Chapman, H. S. Taylor, A. J. Allmand, J. A. Christiansen, E. J. Bowen, W. A. Noyes, O. Stern, R. G. W. Norrish, B. Flurscheim, A. L. Marshall, Part II.: The mechanism of photochemical reactions. general discussion, Transactions of the Faraday Society 21 (1926) 581–590. `doi:10.1039/TF9262100581`.
URL `http://dx.doi.org/10.1039/TF9262100581`

[3] E. U. Condon, A theory of intensity distribution in band systems, Physical Review 28 (6) (1926) 1182–1201. doi:10.1103/PhysRev.28.1182.
URL http://link.aps.org/doi/10.1103/PhysRev.28.1182

[4] E. U. Condon, Nuclear motions associated with electron transitions in diatomic molecules, Physical Review 32 (6) (1928) 858–872. doi:10.1103/PhysRev.32.858.
URL http://link.aps.org/doi/10.1103/PhysRev.32.858

[5] T. E. Sharp, H. M. Rosenstock, Franck–condon factors for polyatomic molecules, The Journal of Chemical Physics 41 (11) (1963) 3453–3463. doi:10.1063/1.1725748.
URL http://link.aip.org/link/?JCP/41/3453/1

[6] E. V. Doktorov, I. A. Malkin, V. I. Man'ko, Dynamical symmetry of vibronic transitions in polyatomic molecules and the franck-condon principle, Journal of Molecular Spectroscopy 56 (1) (1975) 1–20. doi:10.1016/0022-2852(75)90199-X.
URL http://dx.doi.org/10.1016/0022-2852(75)90199-X

[7] E. V. Doktorov, I. A. Malkin, V. I. Man'ko, Dynamical symmetry of vibronic transitions in polyatomic molecules and the Franck-Condon principle, Journal of Molecular Spectroscopy 64 (2) (1977) 302–326. doi:10.1016/0022-2852(77)90269-7.
URL http://www.sciencedirect.com/science/article/B6WK8-4CRGB5C-FP/2/cc9f8518cc9b409ac36c83c665da7ea1

[8] P. T. Ruhoff, Recursion relations for multi-dimensional franck-condon overlap integrals, Chemical Physics 186 (2–3) (1994) 355–374. doi:10.1016/0301-0104(94)00173-1.
URL http://www.sciencedirect.com/science/article/pii/0301010494001731

[9] R. Berger, M. Klessinger, Algorithms for exact counting of energy levels of spectroscopic transitions at different temperatures, Journal of Com-

putational Chemistry 18 (10) (1997) 1312–1319. `doi:10.1002/(SICI)1096-987X(19970730)18:10<1312::AID-JCC5>3.0.CO;2-Q`.

[10] J. R. Reimers, A practical method for the use of curvilinear coordinates in calculations of normal-mode-projected displacements and duschinsky rotation matrices for large molecules, The Journal of Chemical Physics 115 (20) (2001) 9103–9109. `arXiv:https://doi.org/10.1063/1.1412875`, `doi:10.1063/1.1412875`.
URL `https://doi.org/10.1063/1.1412875`

[11] M. Dierksen, S. Grimme, Density functional calculations of the vibronic structure of electronic absorption spectra, The Journal of Chemical Physics 120 (8) (2004) 3544–3554. `doi:10.1063/1.1642595`.
URL `http://dx.doi.org/10.1063/1.1642595`

[12] H.-C. Jankowiak, J. L. Stuber, R. Berger, Vibonic transitions in large molecular systems: Rigorous prescreening conditions for franck-condon factors, The Journal of Chemical Physics 127 (2007) 234101.

[13] F. Santoro, R. Improta, A. Lami, J. Bloino, V. Barone, Effective method to compute franck-condon integrals for optical spectra of large molecules in solution, The Journal of Chemical Physics 126 (8) (2007) 084509. `doi:10.1063/1.2437197`.
URL `http://dx.doi.org/10.1063/1.2437197`

[14] M. J. Frisch, G. W. Trucks, H. B. Schlegel, G. E. Scuseria, M. A. Robb, J. R. Cheeseman, G. Scalmani, V. Barone, G. A. Petersson, H. Nakatsuji, X. Li, M. Caricato, A. V. Marenich, J. Bloino, B. G. Janesko, R. Gomperts, B. Mennucci, H. P. Hratchian, J. V. Ortiz, A. F. Izmaylov, J. L. Sonnenberg, D. Williams-Young, F. Ding, F. Lipparini, F. Egidi, J. Goings, B. Peng, A. Petrone, T. Henderson, D. Ranasinghe, V. G. Zakrzewski, J. Gao, N. Rega, G. Zheng, W. Liang, M. Hada, M. Ehara, K. Toyota, R. Fukuda, J. Hasegawa, M. Ishida, T. Nakajima, Y. Honda, O. Kitao, H. Nakai, T. Vreven, K. Throssell, J. A. Montgomery, Jr., J. E. Peralta,

F. Ogliaro, M. J. Bearpark, J. J. Heyd, E. N. Brothers, K. N. Kudin, V. N. Staroverov, T. A. Keith, R. Kobayashi, J. Normand, K. Raghavachari, A. P. Rendell, J. C. Burant, S. S. Iyengar, J. Tomasi, M. Cossi, J. M. Millam, M. Klene, C. Adamo, R. Cammi, J. W. Ochterski, R. L. Martin, K. Morokuma, O. Farkas, J. B. Foresman, D. J. Fox, Gaussian 16 Revision A.03, gaussian Inc. Wallingford CT (2016).

[15] S. G. Balasubramani, G. P. Chen, S. Coriani, M. Diedenhofen, M. S. Frank, Y. J. Franzke, F. Furche, R. Grotjahn, M. E. Harding, C. Hättig, A. Hellweg, B. Helmich-Paris, C. Holzer, U. Huniar, M. Kaupp, A. Marefat Khah, S. Karbalaei Khani, T. Müller, F. Mack, B. D. Nguyen, S. M. Parker, E. Perlt, D. Rappoport, K. Reiter, S. Roy, M. Rückert, G. Schmitz, M. Sierka, E. Tapavicza, D. P. Tew, C. van Wüllen, V. K. Voora, F. Weigend, A. Wodyński, J. M. Yu, TURBOMOLE: Modular program suite for ab initio quantum-chemical and condensed-matter simulations, The Journal of Chemical Physics 152 (18) (2020) 184107. `arXiv:https://doi.org/10.1063/5.0004635`, `doi:10.1063/5.0004635`.
URL `https://doi.org/10.1063/5.0004635`

[16] E. J. Baerends, T. Ziegler, A. J. Atkins, J. Autschbach, O. Baseggio, D. Bashford, A. Bérces, F. M. Bickelhaupt, C. Bo, P. M. Boerrigter, L. Cavallo, C. Daul, D. P. Chong, D. V. Chulhai, L. Deng, R. M. Dickson, J. M. Dieterich, D. E. Ellis, M. van Faassen, L. Fan, T. H. Fischer, A. Förster, C. Fonseca Guerra, M. Franchini, A. Ghysels, A. Giammona, S. J. A. van Gisbergen, A. Goez, A. W. Götz, J. A. Groeneveld, O. V. Gritsenko, M. Grüning, S. Gusarov, F. E. Harris, P. van den Hoek, Z. Hu, C. R. Jacob, H. Jacobsen, L. Jensen, L. Joubert, J. W. Kaminski, G. van Kessel, C. König, F. Kootstra, A. Kovalenko, M. V. Krykunov, E. van Lenthe, D. A. McCormack, A. Michalak, M. Mitoraj, S. M. Morton, J. Neugebauer, V. P. Nicu, L. Noodleman, V. P. Osinga, S. Patchkovskii, M. Pavanello, C. A. Peeples, P. H. T. Philipsen, D. Post, C. C. Pye, H. Ramanantoanina, P. Ramos, W. Ravenek, M. Reimann, J. I. Rodríguez, P. Ros,

R. Rüger, P. R. T. Schipper, D. Schlüns, H. van Schoot, G. Schreckenbach, J. S. Seldenthuis, M. Seth, J. G. Snijders, M. Solà, M. Stener, M. Swart, D. Swerhone, V. Tognetti, G. te Velde, P. Vernooijs, L. Versluis, L. Visscher, O. Visser, F. Wang, T. A. Wesolowski, E. M. van Wezenbeek, G. Wiesenekker, S. K. Wolff, T. K. Woo, A. L. Yakovlev, Adf 2020, sCM, Theoretical Chemistry, Vrije Universiteit, Amsterdam, The Netherlands (2020).
URL `http://www.scm.com`

[17] F. Santoro, $\mathcal{FC}classes$, a fortran 77 code, visit http://village.ipcf.cnr.it (2008).

[18] F. Neese, F. Wennmohs, U. Becker, C. Riplinger, The ORCA quantum chemistry program package, The Journal of Chemical Physics 152 (22) (2020) 224108. `arXiv:https://doi.org/10.1063/5.0004608`, `doi:10.1063/5.0004608`.
URL `https://doi.org/10.1063/5.0004608`

[19] V. A. Mozhayskiy, A. I. Krylov, ezspectrum (2020).
URL `http://iopenshell.usc.edu/downloads`

[20] J. Bloino, M. Biczysko, O. Crescenzi, V. Barone, Integrated computational approach to vibrationally resolved electronic spectra: Anisole as a test case, The Journal of Chemical Physics 128 (24) (2008) 244105. `doi:10.1063/1.2943140`.
URL `http://link.aip.org/link/?JCP/128/244105/1`

[21] M. Biczysko, J. Bloino, V. Barone, First principle simulation of vibrationally resolved $A^2B_1 \leftarrow \tilde{X}^2A_1$ electronic transition of phenyl radical, Chemical Physics Letters 471 (1-3) (2009) 143–147. `doi:10.1016/j.cplett.2009.01.082`.
URL `http://www.sciencedirect.com/science/article/pii/S0009261409001031`

[22] J. Bloino, A. Baiardi, M. Biczysko, Aiming at an accurate prediction of vibrational and electronic spectra for medium-to-large molecules: An overview, International Journal of Quantum Chemistry 116 (21) (2016) 1543–1574. `doi:10.1002/qua.25188`.
URL `http://dx.doi.org/10.1002/qua.25188`

[23] F. Santoro, A. Lami, R. Improta, J. Bloino, V. Barone, Effective method for the computation of optical spectra of large molecules at finite temperature including the duschinsky and herzberg-teller effect: The q_X band of porphyrin as a case study, The Journal of Chemical Physics 128 (22) (2008) 224311. `doi:10.1063/1.2929846`.

[24] F. Egidi, J. Bloino, C. Cappelli, V. Barone, A robust and effective time-independent route to the calculation of resonance raman spectra of large molecules in condensed phases with the inclusion of duschinsky, herzberg–teller, anharmonic, and environmental effects, Journal of Chemical Theory and Computation 10 (1) (2014) 346–363. `doi:10.1021/ct400932e`.
URL `http://pubs.acs.org/doi/abs/10.1021/ct400932e`

[25] A. Baiardi, J. Bloino, V. Barone, A general time-dependent route to resonance-raman spectroscopy including franck-condon, herzberg-teller and duschinsky effects, The Journal of Chemical Physics 141 (11) (2014) 114108. `doi:10.1063/1.4895534`.
URL `http://scitation.aip.org/content/aip/journal/jcp/141/11/10.1063/1.4895534`

[26] M. Fedorovsky, PyVib2, a program for analyzing vibrational motion and vibrational spectra, `http://pyvib2.sourceforge.net` (2007).

[27] D. Licari, A. Baiardi, M. Biczysko, F. Egidi, C. Latouche, V. Barone, Implementation of a graphical user interface for the virtual multifrequency spectrometer: The VMS-Draw tool, Journal of Computational Chemistry 36 (5) (2015) 321–334. `arXiv:https://onlinelibrary.wiley.com/doi/`

`pdf/10.1002/jcc.23785`, `doi:10.1002/jcc.23785`.
URL `https://onlinelibrary.wiley.com/doi/abs/10.1002/jcc.23785`

[28] M. Wakabayashi, S. Yokojima, T. Fukaminato, K.-i. Shiino, M. Irie, S. Nakamura, Anisotropic dissymmetry factor, g: Theoretical investigation on single molecule chiroptical spectroscopy, The Journal of Physical Chemistry A 118 (27) (2014) 5046–5057. `doi:10.1021/jp409559t`.

[29] D. Licari, M. Fusè, A. Salvadori, N. Tasinato, M. Mendolicchio, G. Mancini, V. Barone, Towards the SMART workflow system for computational spectroscopy, Phys. Chem. Chem. Phys. 20 (2018) 26034–26052. `doi:10.1039/C8CP03417F`.

[30] X. Mu, X. Chen, J. Wang, M. Sun, Visualizations of electric and magnetic interactions in electronic circular dichroism and raman optical activity, The Journal of Physical Chemistry A 123 (37) (2019) 8071–8081. `doi:10.1021/acs.jpca.9b06674`.

[31] Q. Yang, M. Fusè, J. Bloino, Theoretical investigation of the circularly polarized luminescence of a chiral boron dipyrromethene (bodipy) dye, Frontiers in Chemistry 8 (2020) 801. `doi:10.3389/fchem.2020.00801`.
URL `https://www.frontiersin.org/article/10.3389/fchem.2020.00801`

[32] M. Lessi, C. Manzini, P. Minei, L. A. Perego, J. Bloino, F. Egidi, V. Barone, A. Pucci, F. Bellina, Synthesis and optical properties of imidazole-based fluorophores having high quantum yields, ChemPlusChem 79 (3) (2014) 366–370. `doi:10.1002/cplu.201300413`.
URL `http://dx.doi.org/10.1002/cplu.201300413`

[33] N. Hellou, M. Srebro-Hooper, L. Favereau, F. Zinna, E. Caytan, L. Toupet, V. Dorcet, M. Jean, N. Vanthuyne, J. A. G. Williams, L. Di Bari, J. Autschbach, J. Crassous, Enantiopure cycloiridiated complexes bearing a pentahelicenic N-heterocyclic carbene and displaying long-lived circularly polarized phosphorescence, Angewandte

Chemie International Edition 56 (28) (2017) 8236–8239. `arXiv:https://onlinelibrary.wiley.com/doi/pdf/10.1002/anie.201704263`, `doi:10.1002/anie.201704263`.
URL `https://onlinelibrary.wiley.com/doi/abs/10.1002/anie.201704263`

[34] H. Yersin, Highly efficient OLEDs with phosphorescent materials, John Wiley & Sons, 2008.

[35] C. Ulbricht, B. Beyer, C. Friebe, A. Winter, U. S. Schubert, Recent developments in the application of phosphorescent iridium (iii) complex systems, Advanced Materials 21 (44) (2009) 4418–4441. `doi:https://doi.org/10.1002/adma.200803537`.

[36] J. M. Hearn, I. Romero-Canelón, B. Qamar, Z. Liu, I. Hands-Portman, P. J. Sadler, Organometallic iridium (iii) anticancer complexes with new mechanisms of action: Nci-60 screening, mitochondrial targeting, and apoptosis, ACS chemical biology 8 (6) (2013) 1335–1343. `doi:https://doi.org/10.1021/cb400070a`.

[37] D.-L. Ma, H. P. Ng, S.-Y. Wong, K. Vellaisamy, K.-J. Wu, C.-H. Leung, Iridium (iii) complexes as reaction based chemosensors for medical diagnostics, Dalton Transactions 47 (43) (2018) 15278–15282. `doi:https://doi.org/10.1039/C8DT03492C`.

[38] E. Marchi, R. Sinisi, G. Bergamini, M. Tragni, M. Monari, M. Bandini, P. Ceroni, Easy separation of δ and λ isomers of highly luminescent [IrIII]-cyclometalated complexes based on chiral phenol-oxazoline ancillary ligands, Chemistry – A European Journal 18 (28) (2012) 8765–8773. `arXiv:https://chemistry-europe.onlinelibrary.wiley.com/doi/pdf/10.1002/chem.201200709`, `doi:10.1002/chem.201200709`.
URL `https://chemistry-europe.onlinelibrary.wiley.com/doi/abs/10.1002/chem.201200709`

[39] L. Ricciardi, M. La Deda, A. Ionescu, N. Godbert, I. Aiello, M. Ghedini, M. Fusè, I. Rimoldi, E. Cesarotti, Luminescent chiral ionic ir(III) complexes: Synthesis and photophysical properties, Journal of Luminescence 170 (2016) 812 – 819, light, Energy and Life. `doi:https://doi.org/10.1016/j.jlumin.2015.08.003`.
URL `http://www.sciencedirect.com/science/article/pii/S0022231315004354`

[40] G. Mazzeo, M. Fusè, G. Longhi, I. Rimoldi, E. Cesarotti, A. Crispini, S. Abbate, Vibrational circular dichroism and chiroptical properties of chiral ir(III) luminescent complexes, Dalton Trans. 45 (2016) 992–999. `doi:10.1039/C5DT03642A`.
URL `http://dx.doi.org/10.1039/C5DT03642A`

[41] D. R. Martir, C. Momblona, A. Pertegás, D. B. Cordes, A. M. Z. Slawin, H. J. Bolink, E. Zysman-Colman, Chiral iridium(III) complexes in light-emitting electrochemical cells: Exploring the impact of stereochemistry on the photophysical properties and device performances, ACS Applied Materials & Interfaces 8 (49) (2016) 33907–33915. `doi:10.1021/acsami.6b14050`.

[42] R. Manguin, D. Pichon, R. Tarrieu, T. Vives, T. Roisnel, V. Dorcet, C. Crévisy, K. Miqueu, L. Favereau, J. Crassous, M. Mauduit, O. Baslé, A kinetic resolution strategy for the synthesis of chiral octahedral NHC–iridium(III) catalysts, Chem. Commun. 55 (2019) 6058–6061. `doi:10.1039/C9CC02434D`.
URL `http://dx.doi.org/10.1039/C9CC02434D`

[43] V. Barone, J. Bloino, M. Biczysko, F. Santoro, Fully integrated approach to compute vibrationally resolved optical spectra: From small molecules to macrosystems, Journal of Chemical Theory and Computation 5 (3) (2009) 540–554. `doi:10.1021/ct8004744`.

[44] J. Bloino, M. Biczysko, F. Santoro, V. Barone, General approach to compute vibrationally resolved one-photon electronic spectra, Journal of Chemical Theory and Computation 6 (4) (2010) 1256–1274. `doi:10.1021/ct9006772`.
URL `http://dx.doi.org/10.1021/ct9006772`

[45] A. Baiardi, J. Bloino, V. Barone, General time dependent approach to vibronic spectroscopy including franck–condon, herzberg–teller, and duschinsky effects, Journal of Chemical Theory and Computation 9 (9) (2013) 4097–4115. `doi:10.1021/ct400450k`.
URL `http://pubs.acs.org/doi/abs/10.1021/ct400450k`

[46] A. Baiardi, J. Bloino, V. Barone, General formulation of vibronic spectroscopy in internal coordinates, The Journal of Chemical Physics 144 (8) (2016) 084114. `doi:10.1063/1.4942165`.
URL `http://scitation.aip.org/content/aip/journal/jcp/144/8/10.1063/1.4942165`

[47] V. Barone, A. Baiardi, M. Biczysko, J. Bloino, C. Cappelli, F. Lipparini, Implementation and validation of a multi-purpose virtual spectrometer for large systems in complex environments, Physical Chemistry Chemical Physics 14 (36) (2012) 12404–12422. `doi:10.1039/C2CP41006K`.
URL `http://dx.doi.org/10.1039/C2CP41006K`

[48] A. O. Mitrushchenkov, A new general renner-teller (including $\epsilon \gtrsim 1$) spectroscopic formalism for triatomic molecules, The Journal of Chemical Physics 136 (2) (2012) 024108. `doi:10.1063/1.3672162`.
URL `https://doi.org/10.1063/1.3672162`

[49] S. N. Yurchenko, L. Lodi, J. Tennyson, A. V. Stolyarov, Duo: A general program for calculating spectra of diatomic molecules, Computer Physics Communications 202 (2016) 262–275. `doi:https://doi.org/10.1016/j.cpc.2015.12.021`.

URL `http://www.sciencedirect.com/science/article/pii/S0010465516000023`

[50] H. Köppel, W. Domcke, L. S. Cederbaum, Multimode molecular dynamics beyond the born-oppenheimer approximation, in: I. Prigogine, S. A. Rice (Eds.), Advances in Chemical Physics, Vol. 57, Wiley-Blackwell, 1984, pp. 59–246. `doi:10.1002/9780470142813.ch2`.
URL `http://dx.doi.org/10.1002/9780470142813.ch2`

[51] S. M. Rabidoux, V. Eijkhout, J. F. Stanton, Parallelization strategy for large-scale vibronic coupling calculations, The Journal of Physical Chemistry A 118 (51) (2014) 12059–12068. `arXiv:https://doi.org/10.1021/jp507880q`, `doi:10.1021/jp507880q`.
URL `https://doi.org/10.1021/jp507880q`

[52] J. Cerezo, F. J. Avila Ferrer, G. Prampolini, F. Santoro, Modeling solvent broadening on the vibronic spectra of a series of coumarin dyes. from implicit to explicit solvent models, Journal of Chemical Theory and Computation 11 (12) (2015) 5810–5825. `arXiv:https://doi.org/10.1021/acs.jctc.5b00870`, `doi:10.1021/acs.jctc.5b00870`.
URL `https://doi.org/10.1021/acs.jctc.5b00870`

[53] J. Liu, W. Liang, Analytical approach for the excited-state hessian in time-dependent density functional theory: Formalism, implementation, and performance, The Journal of Chemical Physics 135 (18) (2011) 184111. `doi:10.1063/1.3659312`.
URL `http://link.aip.org/link/?JCP/135/184111/1`

[54] F. Egidi, D. B. Williams-Young, A. Baiardi, J. Bloino, G. Scalmani, M. J. Frisch, X. Li, V. Barone, Effective inclusion of mechanical and electrical anharmonicity in excited electronic states: Vpt2-tddft route, Journal of Chemical Theory and Computation 13 (6) (2017) 2789–2803. `doi:10.1021/acs.jctc.7b00218`.
URL `http://dx.doi.org/10.1021/acs.jctc.7b00218`

[55] P. Macak, Y. Luo, H. Ågren, Simulations of vibronic profiles in two-photon absorption, Chemical Physics Letters 330 (3–4) (2000) 447–457. `doi:10.1016/S0009-2614(00)01096-4`.

[56] D. C. Blazej, W. L. Peticolas, Ultraviolet resonance raman excitation profiles of pyrimidine nucleotides, The Journal of Chemical Physics 72 (5) (1980) 3134–3142. `doi:10.1063/1.439547`.
URL `http://scitation.aip.org/content/aip/journal/jcp/72/5/10.1063/1.439547`

[57] G. Herzberg, E. Teller, Schwingungsstruktur der elektronenübergänge bei mehratomigen molekülen, Zeitschrift für Physikalische Chemie - Abteilung B 21 (1933) 410–446.

[58] F. Duschinsky, On the interpretation of electronic spectra of polyatomic molecules. i. concerning the franck-condon principle, Acta Physicochimica URSS 7 (1937) 551–566.

[59] J. Cerezo, J. Zúñiga, A. Requena, F. J. Ávila Ferrer, F. Santoro, Harmonic models in cartesian and internal coordinates to simulate the absorption spectra of carotenoids at finite temperatures, Journal of Chemical Theory and Computation 9 (11) (2013) 4947–4958. `doi:10.1021/ct4005849`.
URL `https://doi.org/10.1021/ct4005849`

[60] K. Burke, Perspective on density functional theory, The Journal of chemical physics 136 (15) (2012) 150901.

[61] K. Burke, J. Werschnik, E. Gross, Time-dependent density functional theory: Past, present, and future, The Journal of chemical physics 123 (6) (2005) 062206.

[62] M. E. Casida, Time-dependent density-functional theory for molecules and molecular solids, J. Mol. Struct. Theochem 914 (1-3) (2009) 3–18.

[63] G. Scalmani, M. J. Frisch, B. Mennucci, J. Tomasi, R. Cammi, V. Barone, Geometries and properties of excited states in the gas phase and in solution:

Theory and application of a time-dependent density functional theory polarizable continuum model, The Journal of Chemical Physics 124 (9) (2006) 094107. `doi:10.1063/1.2173258`.
URL `http://link.aip.org/link/?JCP/124/094107/1`

[64] S. Grimme, J. Antony, S. Ehrlich, H. Krieg, A consistent and accurate ab initio parametrization of density functional dispersion correction (dft-d) for the 94 elements h-pu, The Journal of Chemical Physics 132 (15) (2010) 154104. `doi:10.1063/1.3382344`.
URL `http://scitation.aip.org/content/aip/journal/jcp/132/15/10.1063/1.3382344`

[65] S. Grimme, S. Ehrlich, L. Goerigk, Effect of the damping function in dispersion corrected density functional theory, Journal of Computational Chemistry 32 (7) (2011) 1456–1465. `doi:10.1002/jcc.21759`.
URL `http://dx.doi.org/10.1002/jcc.21759`

[66] J. Tomasi, B. Mennucci, R. Cammi, Quantum mechanical continuum solvation models, Chemical Reviews 105 (8) (2005) 2999–3094. `doi:10.1021/cr9904009`.
URL `http://pubs.acs.org/doi/abs/10.1021/cr9904009`

[67] E. Cancès, B. Mennucci, J. Tomasi, A new integral equation formalism for the polarizable continuum model: Theoretical background and applications to isotropic and anisotropic dielectrics, The Journal of Chemical Physics 107 (8) (1997) 3032–3041. `doi:10.1063/1.474659`.
URL `http://scitation.aip.org/content/aip/journal/jcp/107/8/10.1063/1.474659`

[68] M. Cossi, V. Barone, Time-dependent density functional theory for molecules in liquid solutions, The Journal of chemical physics 115 (10) (2001) 4708–4717.

[69] A. D. Becke, Density-functional exchange-energy approximation with correct asymptotic behavior, Physical review A 38 (6) (1988) 3098.

[70] J. P. Perdew, K. Burke, Y. Wang, Generalized gradient approximation for the exchange-correlation hole of a many-electron system, Physical Review B 54 (23) (1996) 16533.

[71] C. Adamo, V. Barone, Toward reliable density functional methods without adjustable parameters: The pbe0 model, The Journal of Chemical Physics 110 (13) (1999) 6158–6170. `doi:10.1063/1.478522`.
URL `http://link.aip.org/link/doi/10.1063/1.478522`

[72] O. A. Vydrov, G. E. Scuseria, Assessment of a long-range corrected hybrid functional, Journal of Chemical Physics 125 (2006) 234109.

[73] S. Y. Haoyu, X. He, S. L. Li, D. G. Truhlar, Mn15: A kohn–sham global-hybrid exchange–correlation density functional with broad accuracy for multi-reference and single-reference systems and noncovalent interactions, Chemical science 7 (8) (2016) 5032–5051.

[74] Y. Zhao, N. E. Schults, D. G. Truhlar, Design of density functionals by combining the method of constraint satisfaction with parametrization for thermochemistry, thermochemical kinetics, and noncovalent interactions, J. Chem. Theory Comput. 2 (2006) 364–382.

[75] Y. Zhao, D. G. Truhlar, The m06 suite of density functionals for main group thermochemistry, thermochemical kinetics, noncovalent interactions, excited states, and transition elements: Two new functionals and systematic testing of four m06-class functionals and 12 other functionals, Theor. Chem. Acc. 120 (2008) 215–241.

[76] V. Barone, M. Biczysko, J. Bloino, Fully anharmonic ir and raman spectra of medium-size molecular systems: accuracy and interpretation, Physical Chemistry Chemical Physics 16 (5) (2014) 1759–1787. `doi:10.1039/C3CP53413H`.
URL `http://dx.doi.org/10.1039/C3CP53413H`

[77] V. Barone, J. Bloino, M. Biczysko, Validation of the dft/n07d computational model on the magnetic, vibrational and electronic properties of vinyl radical, Physical Chemistry Chemical Physics 12 (5) (2010) 1092–1101. `doi:10.1039/B915246F`.
URL `http://dx.doi.org/10.1039/B915246F`

[78] F. Jensen, Unifying general and segmented contracted basis sets. segmented polarization consistent basis sets, Journal of chemical theory and computation 10 (3) (2014) 1074–1085.

[79] C. Kumar, H. Fliegl, F. Jensen, A. M. Teale, S. Reine, T. Kjærgaard, Accelerating kohn-sham response theory using density fitting and the auxiliary-density-matrix method, International Journal of Quantum Chemistry 118 (16) (2018) e25639.

[80] T. H. Dunning, Gaussian basis sets for use in correlated molecular calculations. i. the atoms boron through neon and hydrogen, J. Chem. Phys. 90 (2) (1989) 1007–1023. `doi:10.1063/1.456153`.
URL `https://doi.org/10.1063/1.456153`

[81] E. Papajak, J. Zheng, X. Xu, H. R. Leverentz, D. G. Truhlar, Perspectives on basis sets beautiful: Seasonal plantings of diffuse basis functions, J. Chem. Theory Comput. 7 (10) (2011) 3027–3034. `doi:10.1021/ct200106a`.
URL `https://doi.org/10.1021/ct200106a`

[82] P. J. Hay, W. R. Wadt, Ab initio effective core potentials for molecular calculations. potentials for the transition metal atoms sc to hg, The Journal of chemical physics 82 (1) (1985) 270–283.

[83] P. Fuentealba, H. Preuss, H. Stoll, L. Von Szentpály, A proper account of core-polarization with pseudopotentials: single valence-electron alkali compounds, Chemical Physics Letters 89 (5) (1982) 418–422.

[84] M. Fusè, F. Egidi, J. Bloino, Vibrational circular dichroism under the quantum magnifying glass: from the electronic flow to the spectroscopic observable, Physical Chemistry Chemical Physics 21 (8) (2019) 4224–4239. `doi:10.1039/C8CP06514D`.
URL `http://dx.doi.org/10.1039/C8CP06514D`

[85] H. Lu, J. Mack, T. Nyokong, N. Kobayashi, Z. Shen, Optically active bodipys, Coordination Chemistry Reviews 318 (2016) 1–15. `doi:https://doi.org/10.1016/j.ccr.2016.03.015`.
URL `http://www.sciencedirect.com/science/article/pii/S0010854515301466`

[86] F. Santoro, A. Lami, R. Improta, V. Barone, Effective method to compute vibrationally resolved optical spectra of large molecules at finite temperature in gas phase and in solution, The Journal of Chemical Physics 126 (18) (2007) 184102. `doi:10.1063/1.2721539`.

[87] M. J. Frisch, G. W. Trucks, H. B. Schlegel, G. E. Scuseria, M. A. Robb, J. R. Cheeseman, G. Scalmani, V. Barone, G. A. Petersson, H. Nakatsuji, X. Li, M. Caricato, A. V. Marenich, J. Bloino, B. G. Janesko, R. Gomperts, B. Mennucci, H. P. Hratchian, J. V. Ortiz, A. F. Izmaylov, J. L. Sonnenberg, D. Williams-Young, F. Ding, F. Lipparini, F. Egidi, J. Goings, B. Peng, A. Petrone, T. Henderson, D. Ranasinghe, V. G. Zakrzewski, J. Gao, N. Rega, G. Zheng, W. Liang, M. Hada, M. Ehara, K. Toyota, R. Fukuda, J. Hasegawa, M. Ishida, T. Nakajima, Y. Honda, O. Kitao, H. Nakai, T. Vreven, K. Throssell, J. A. Montgomery Jr., J. E. Peralta, F. Ogliaro, M. J. Bearpark, J. J. Heyd, E. N. Brothers, K. N. Kudin, V. N. Staroverov, T. A. Keith, R. Kobayashi, J. Normand, K. Raghavachari, A. P. Rendell, J. C. Burant, S. S. Iyengar, J. Tomasi, M. Cossi, J. M. Millam, M. Klene, C. Adamo, R. Cammi, J. W. Ochterski, R. L. Martin, K. Morokuma, O. Farkas, J. B. Foresman, D. J. Fox, Gaussian development version, revision j.05Gaussian, Inc., Wallingford CT (2019).

[88] F. Jensen, Polarization consistent basis sets: Principles, The Journal of Chemical Physics 115 (20) (2001) 9113–9125. `doi:10.1063/1.1413524`. URL `https://doi.org/10.1063/1.1413524`

[89] V. Barone, M. Biczysko, M. Borkowska-Panek, J. Bloino, A multifrequency virtual spectrometer for complex bio-organic systems: Vibronic and environmental effects on the UV/Vis spectrum of chlorophyll a, ChemPhysChem 15 (15) (2014) 3355–3364. `arXiv:https://chemistry-europe.onlinelibrary.wiley.com/doi/pdf/10.1002/cphc.201402300`, `doi:10.1002/cphc.201402300`. URL `https://chemistry-europe.onlinelibrary.wiley.com/doi/abs/10.1002/cphc.201402300`

[90] B. Minaev, Y.-H. Wang, G.-K. Wang, Y. Luo, H. Ågren, Spectrochimica Acta Part A: Molecular Spectroscopy 65 (2006) 308.

[91] L. A. Nafie, Molecular Electronic Transition Current Density, 1994, Ch. 4, pp. 63–80. `arXiv:https://pubs.acs.org/doi/pdf/10.1021/ba-1994-0240.ch004`, `doi:10.1021/ba-1994-0240.ch004`. URL `https://pubs.acs.org/doi/abs/10.1021/ba-1994-0240.ch004`

[92] L. A. Nafie, Electron transition current density in molecules. 1. non-born-oppenheimer theory of vibronic and vibrational transitions, J. Phys. Chem. A 101 (42) (1997) 7826–7833. `doi:10.1021/jp9706137`.

[93] A. C. Telea, Data visualization: principles and practice, AK Peters/CRC Press, 2007.

[94] R. F. W. Bader, A quantum theory of molecular structure and its applications, Chemical Reviews 91 (5) (1991) 893–928. `doi:10.1021/cr00005a013`.

[95] L. A. Nafie, Vibrational Optical Activity: Principles and Applications, John Wiley & Sons, Ltd, 2011. URL `http://onlinelibrary.wiley.com/book/10.1002/9781119976516`